Sub-second Nanocomposite Synthesis in Continuous Flow Supercritical CO_2 Reactor

Mohammad Masrur Hossain

A thesis

submitted in partial fulfillment of the

requirements for the degree of

MASTER OF SCIENCE IN MECHANICAL ENGINEERING

University of Washington

2023

Reading Committee:

Igor Novosselov, Chair

John Kramlich
Juan Carlos Idrobo

Program Authorized to Offer Degree:

Mechanical Engineering

University of Washington

Abstract

Sub-second Nanocomposite Synthesis in Continuous Flow Supercritical CO_2 Reactor

Mohammad Masrur Hossain

Chair of the Supervisory Committee:
Research Associate Professor Igor Novosselov
Department of Mechanical Engineering

Metal-organic frameworks (MOFs) have attracted considerable scientific attention due to their diverse potential applications. However, to be viable for large-scale industrial use, MOFs must exhibit the intended functionality and properties and be produced and processed in an economically scalable manner that yields high-quality products with minimal environmental impact. In light of growing environmental concerns and commercial constraints, synthetic methods must prioritize eco-friendliness.

This dissertation presents a method for synthesizing MOF composites using supercritical fluid as a reaction medium and a continuous flow process with short residence times. In the supercritical phase, fluids exhibit high sensitivity to minor changes in temperature or pressure, which can result in significant alterations in their thermophysical properties. This characteristic provides an exceptional opportunity to improve heat transfer in a mixing environment for synthesizing the nanocomposite. The use of this method enables a more efficient and environmentally friendly route to scale up the production of MOFs, incorporating principles of Green Chemistry.

The initial focus of this dissertation is the refinement of a continuous flow supercritical reactor for synthesizing HKUST-1, a type of copper-based MOF. This research has led to the fastest-ever reported the synthesis of HKUST-1 in the scientific literature. Expanding upon the work with the continuous flow $scCO_2$ reactor, the second part of this dissertation involved the synthesis of GO@HKUST-1 and CNT@HKUST-1 composite materials using the optimized continuous flow $scCO_2$ reactor. The production rate achieved was multiple magnitudes greater than previous state-of-the-art methods. Moreover, a detailed mechanistic study comprising five experiments was conducted to investigate the impact of $scCO_2$ injection temperature variation on the properties of GO@HKUST-1 and CNT@HKUST-1.

ACKNOWLEDGEMENTS

The successful end of this dissertation is a tribute to the excellent help and steady support of a number of people and institutions. Before I say anything else, I want to thank my co-advisors, Igor Novosselov, John Kramlich, and Juan Carlos Idrobo. Their mentoring, guidance, and wise advice have been like a lighthouse in the dark, choppy waters of academic research.

Their unwavering commitment, careful attention to every detail, and constant support have been the main reasons for my success. Their unwavering dedication to doing the best has made me want to do nothing less than the best. This dissertation would have never been written without their wise advice and guidance. It was a huge job that needed the help of a team of experts, and I will always be grateful for what they did.

The Clean Energy Institute (CEI) at the University of Washington was crucial in making this research happen. Their unwavering support gave me hope and led me to the finish line. I want to thank the leaders and administrative staff of CEI from the bottom of my heart for making this work possible.

But it wasn't just the guidance and direction of the CEI that made this research possible. Under the direction of the one and only Bob Scott, the University of Washington Machine Shop's knowledgeable and patient staff brought this project to life. Their expertise and on-campus presence were the glue that held everything together. And let's not forget the University of Washington Molecular Analysis Facility staff, including Ellen Lavoie, Scott Braswell, and Samantha Young. Their invaluable training and assistance with TEM, SEM, and XRD analysis made all the difference, and their aid was indispensable to this work.

The path toward completion wasn't easy, but the staff at the Washington Clean Energy Testbeds, including the venerable Dr. Michael Pomfret and Dr. Philip Cox, were there every

step of the way. Even during a global pandemic, they always helped me and gave me the tools I needed to keep progressing. Their assistance was deeply appreciated and will not be forgotten. Indeed, this project was a collaborative effort that brought together the best and brightest minds, and for that, I am eternally grateful.

My colleagues in the lab have been nothing short of a lifeline for me. Their unwavering dedication, relentless support, and constant motivation have been the bedrock upon which my personal and professional growth has flourished. And then there's Conrad Austin. His assistance, instruction, and unwavering support have been the wind beneath my wings, propelling me toward the finish line. From the beginning, Conrad has been an essential collaborator, and I am forever indebted to him for his time, expertise, and contributions.

And yet, there is one group of people whose importance in my journey cannot be overstated: my family and friends. They have stood by me through thick and thin, providing the unwavering support, encouragement, and motivation that have kept me going through the most challenging times. Their guidance has been my guiding light, and their love has been my shield against the harsh realities of life. I will always be thankful that they are in my life, and I value their constant support.

To sum up, I will always owe a lot to these respected mentors. Their excellent advice and help have been the foundation of my academic success. Their profound impact on my life and career is something that I will always cherish and hold close to my heart.

Table of Contents

List Of Figures

List Of Tables

Chapter 1 Introduction

Metal-organic frameworks (MOFs) have gained substantial scientific attention due to their extensive potential applications in various fields, such as gas storage [1, 2], separation [3], catalysis [4, 5], drug delivery [6], conducting [7], and electronic materials [8]. The ability of MOFs to store and purify fuel and exhaust gases is particularly intriguing. [1, 9, 10]

For industrial purposes, MOFs must possess specific functionalities and properties that are cost-effective and scalable to produce high-purity products. [11, 12] The increasing awareness of environmental sustainability and commercial constraints has made it crucial for the synthesis processes of MOFs to be eco-friendly. [13] To be considered for industrial applications, the long-term stability of MOFs under realistic conditions, including chemical [14] and thermal stability [14, 15], must be investigated. Developing efficient methods for the large-scale production of MOFs is also essential for their availability in real-life industrial settings. [11, 12] Given the diverse range of potential applications, numerous MOFs must be produced on a large scale, and versatile production methods could facilitate this expansion. [11, 12]

The synthesis of MOFs typically involves long reaction times, ranging from several days to weeks, with slow heating and cooling rates using solvents such as N, N′ - dimethylformamide (DMF), which is toxic and environmentally hazardous. [16, 17] In contrast, hydrothermal syntheses are typically carried out at temperatures up to 220 °C, while microwave [18], sonication [19], and mechanochemical [20] syntheses sometimes involve shorter reaction times. However, for microwave and alternative synthesis methods to be cost-effective for scale-up, they must offer clear benefits over conventional heating routes [21]. It is essential to consider the environmental impact and safety of the solvents and methods used in MOF synthesis. [22] Alternative, eco-friendly methods for MOF synthesis are being

explored to minimize the use of hazardous solvents and reduce the overall environmental impact of the process. [23] These methods can potentially increase the scalability of MOF production while maintaining the desired properties and functionalities required for various industrial applications [24].

To encourage widespread adoption, it is necessary to develop large-scale manufacturing methods for MOF synthesis that are rapid, environmentally friendly, and economically beneficial. [25] Alternative methods have been created to address the limitations of the solvothermal approach and produce MOFs in commercially significant quantities. [26] These techniques have enabled the production of MOFs with desirable characteristics and functions for various industrial applications on a large scale. [27] Continuous-flow methods are desirable for industrial production compared to batch reactors. [28] Continuous flow chemistry is a versatile technique that can be used with a wide range of laboratory syntheses and potentially facilitate the large-scale production of MOFs. [29] Investigating the potential of continuous flow chemistry in MOF synthesis for industrial applications is essential. [30]

Each MOF synthesis method has its benefits and drawbacks. Rubio-Martinez et al. recently published a review of various synthesis methods, including a discussion of the advantages and disadvantages of each approach. [31] Among these methods, MOF synthesis in a supercritical environment appears to be a promising scalable manufacturing method. [32] Compared to other continuous-flow methods, production rates are over ten times higher, and synthesis occurs in seconds instead of tens of hours. [33]

Using a supercritical environment is attractive for MOF synthesis because the thermodynamic properties of the solvent vary significantly with minor changes in pressure or temperature near the critical point.[34] This tunability can influence nanoparticle nucleation. [34] Water (H_2O) has been the preferred supercritical fluid for nanomaterial synthesis, including MOFs. [35]

However, a drawback of supercritical water (scH_2O) is its high critical temperature and pressure values (T = 620 K, P = 22.1 MPa), which leads to high process energy consumption and expensive construction materials. [36] Moreover, the high critical temperature of scH_2O can cause thermal degradation of some MOF precursor materials, such as N, N-dimethylformamide (DMF), which decomposes at about T = 623 K, causing defects in MOF ligands. Additionally, precursor materials in scH_2O are vulnerable to hydrolysis degradation, which restricts the ability of scH_2O-based continuous-flow reactors to synthesize a broad range of MOFs. [37] Thus most common uses for scH_2O are in the gasification application [38-41] and the treatment of recalcitrant organic wastes [42-47].

In contrast to scH_2O, supercritical carbon dioxide ($scCO_2$) has a lower critical point (T = 304 K, P = 7.31 MPa). [48] This means that MOF synthesis using $scCO_2$ requires less energy, has a lower reactor construction cost and avoids the precursor degradation issues associated with scH_2O. [49] Another benefit of $scCO_2$ systems is that they enable the natural separation of the MOF from the effluent, which makes it easy to recycle solvents and reduce waste streamflow. In this study, we utilized $scCO_2$ for large-scale continuous-flow MOF synthesis to address the limitations of scH_2O. [50]

In a recent batch process, $scCO_2$ was utilized to synthesize MOFs. However, this method was not continuous and had long reaction times ranging from 3 to 90 hours. [51] In contrast, continuous-flow processes require careful management of phase changes that occur within the reactor. [52, 53] Moreover, since the thermodynamic properties vary considerably near the critical point, design decisions must consider these nonlinearities to avoid unsafe and unsuccessful reactor operations. [53] To facilitate MOF synthesis rapidly, it is essential to optimize the thermal and mass transfer between the $scCO_2$ and MOF precursor materials. Therefore, the design of the mixer and optimization of the synthesis conditions are crucial for successful and safe continuous-flow MOF synthesis. [49]

This thesis aims to optimize an environmentally friendly system that uses $scCO_2$ as a quick heating and mixing medium for MOF synthesis in a continuous-flow reactor that can be scaled up. This involves two main objectives: (1) the assessment and improvement of the mixer section of the reactor and (2) the demonstration of MOF synthesis within the reactor and conducting of material characterization.

This dissertation is divided into seven chapters. Chapter 1 introduces the research, including the background, motivation, and organization of the thesis. Chapter 2 demonstrates the feasibility of synthesizing high-quality MOFs within sub-second time frames, emphasizing the need to optimize the continuous flow process for HKUST-1 and other MOFs. Chapter 3 elaborates on the continuous flow $scCO_2$ MOF synthesis reactor method and its ability to synthesize the copper and graphene oxide (GO) based MOF composite GO@HKUST-1 across a range of five experiments, thus proving the method's robustness. Chapter 4 highlights the $scCO_2$ method's capability to produce the CNT@HKUST-1 composite. Chapter 5 summarizes the research contributions, while Chapter 6 highlights potential future research directions and outlines recommendations for the scalable and sustainable synthesis of nanoparticles using supercritical phase in continuous flow reactors. Chapter 7 contains the bibliography of all the references cited in this dissertation. It lists all the sources used in the research, including books, articles, journals, and other materials. The bibliography provides complete and accurate information for each source, including the author's name, the title of the work, the publication date, and the publisher or source. The bibliography is valuable for readers who wish to explore the sources further.

Chapter 2 Sub-second HKUST-1 Synthesis in Continuous Flow Supercritical CO_2 Reactor

2.1 Introduction

MOFs are a class of porous coordination polymers with characteristics such as high surface areas and adjustable pore sizes. To date, over 500,000 MOFs have been proposed and synthesized. [54] Unlike conventional porous solid adsorbents, such as activated carbon, zeolites, and N-doped porous carbons [55, 56], MOFs can be used for gas separation and storage due to their controlled pore size, high permeability, and high surface area. [57-59] HKUST-1($Cu_3(BTC)_2$) is one of the most widely studied MOFs, first reported by Chui et al. in 1999. [60] HKUST-1 has garnered significant attention for its potential in various applications, including carbon dioxide captures [61] and hydrogen storage. [9, 62]

The physicochemical properties and eventual practical use of MOFs are closely tied to their morphology. [63, 64] The morphological features depend on the experimental parameters such as synthesis temperature, time, and the stoichiometry of the reagents. [65-67] Rapid, eco-friendly, and scalable MOF synthesis is needed to advance practical implementation. Using supercritical fluids (SCFs) as synthesis environments is a promising approach due to the tunable properties of supercritical fluids and their non-toxic nature. [68-70] The SCFs exhibit gaseous- and liquid-like properties, enabling efficient mixing of the organic compound for various applications [38], including synthesizing several material types. [71, 72] In particular, $scCO_2$ has attracted considerable interest [49] since the synthesis requires low energy consumption (T_{cr} = 304.1°K, P_{cr} = 7.38 MPa) and its antisolvent properties that can enable reusing the solvents and, in turn, reducing the amount of waste stream. [73]

One of the challenges facing the practical application of MOFs is the lack of scalability of the laboratory methods used for their discovery, making it challenging to translate the process from the laboratory to an industrially viable process. [11, 74-77] Shifting from the batch process to continuous flow reactors could be a promising scale-up path [78, 79]; however, preserving the quality of MOFs in the high-throughput synthesis can present a challenge. Rasmussen et al. demonstrated the feasibility of producing high-quality HKUST-1 and UIO-66 MOFs in a continuous flow $scCO_2$ reactor. [49, 73] Their findings indicate in the single-phase conditions are met, the $scCO_2$ environment eliminates the diffusion limitations of reactions in liquid media and multiphase flows, allowing the synthesis of HKUST-1 within a short residence time (τ_{res} = 70 - 170 sec). However, the authors did not investigate the extended range of synthesis temperatures or shorter τ_{res}. Among the unanswered question are (i) what is the limiting operating envelope for HKUST-1 MOF synthesis, and (ii) are there optimal conditions for the production of MOF? This chapter reports the impact of synthesis temperature by systematically varying the $scCO_2$ injection temperature in a sub-second residence time reactor.

2.2 Experimental section

2.2.1 Continuous flow $scCO_2$ reactor

The continuous-flow metal-organic framework (MOF) synthesis reactor, depicted in Figure 2 - 1, can be operated on a temperature range of 298-873K (25-600°C) and a pressure range of 0.101-30 MPa. The reactor employs a three-stream approach, incorporating an unheated metal precursor, an unheated organic precursor, and a heated $scCO_2$ stream. The streams proceed to the counterflow mixing section. The mixing section is designed to optimize the mixing rate, thereby accelerating the process of heating the reagents with $scCO_2$. Upon exiting the counterflow mixing section, the effluent is cooled to ambient temperatures and subsequently directed through a back pressure regulator. The reaction products, including the MOFs, are collected in the liquid phase, and the CO_2 is safely exhausted to a fume hood.

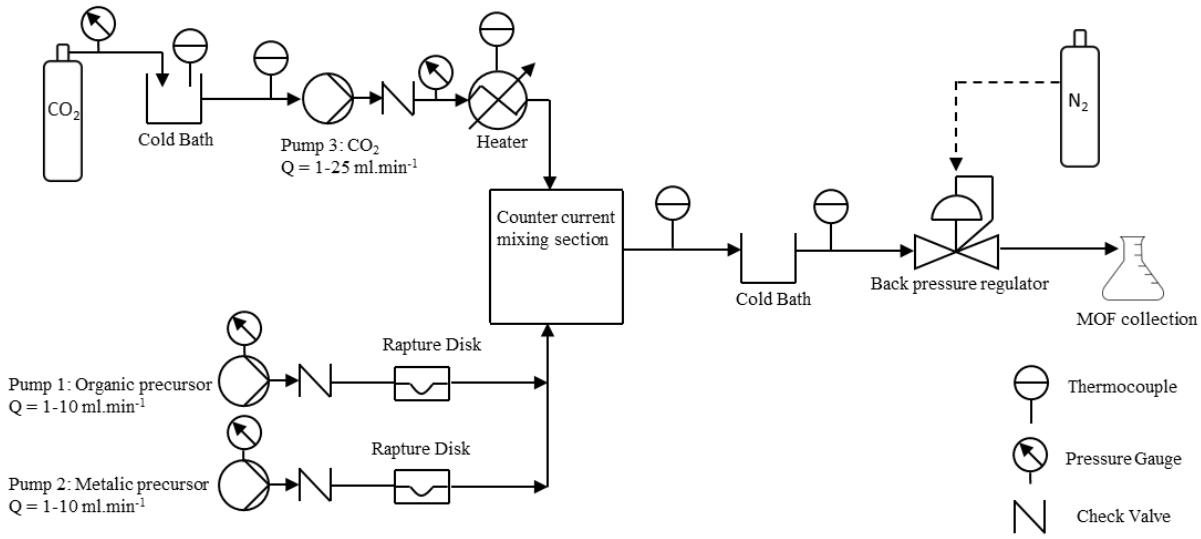

Figure 2 - 1: Design of a $scCO_2$ reactor for HKUST-1, a Cu-based MOF synthesis. Components and instrumentation include a CO_2 tank, cold bath, high-pressure pump, preheater, counter-current mixing chamber, thermocouple, and back pressure regulator.

2.2.2 Materials and preparation method

The chemicals used in this experiment were procured from Sigma-Aldrich and stored following the manufacturer's guidelines. The preparation of the precursor materials was performed as previously reported. [73] Ethanol (EtOH) was used to prepare solutions of 0.24 M Benzene - 1, 3, 5 - tricarboxylic acid (BTC) and 0.1 M Copper (II) nitrate trihydrate, $Cu(NO_3)_2 \cdot 3H_2O$. The precursor concentration was constant. The resultant MOF particles were separated by centrifugation (9,000 rpm for 10 mins) using an Allegra X-30 centrifuge from Bechman Coulter. The MOFs were stored in glass vials and dried at 393°C overnight.

2.2.3 Experiment Conditions

Fourteen experiments were performed to investigate the impact of synthesis temperature on the crystallinity, physisorption, and morphology of HKUST-1. The $scCO_2$ injection temperature was systematically varied between 50°C and 350°C. The flow rates of the precursors were kept the same. The residence times were calculated based on the reactor volume and the supercritical CO_2 density (τ_{res} = ~650 ms). The reactor pressure was maintained at a constant P = 10 MPa.

2.3 Results & discussion

The purity of the crystalline phases in HKUST-1 was evaluated using PXRD (D8 Advance, Bruker) with an IμS 1-D detector. The instrument was operated at a voltage of 40 kV and a current of 40 mA, utilizing CuKα (λ=1.5418Å) radiation, at room temperature over the angular range of 2Θ = 5 ° - 45 °, with a scanning rate of 2° per min. The PXRD peaks in Figure 2 - 2 demonstrate a match with the library HKUST-1 spectra for T_{inj} = 50°C - 250°C. The peaks are concentrated at lower 2Θ angles indicating the microporous nature of the materials. However, at higher synthesis temperatures T > 250ºC, additional peaks (2Θ = 35, 40) is observed due to the formation of copper oxide (CuO); these peaks align with previously reported data.[9, 80] Figure 2 - 2 shows that the crystallinity of the HKUST-1 remained consistent up to T_{inj} = 250 °C. However, increasing the maximum local temperature, e.g., T_{inj} = 350 °C, led to MOFs (or precursors) oxidation-producing CuO. Note that thermogravimetric analysis (TGA) also confirms the destruction of the BTC linker at T~ 340 °C; see Figure 2 - 4. The presence of CuO can significantly impact the physisorption properties, as it may remain within the pores of the framework, leading to a decrease in specific surface area.

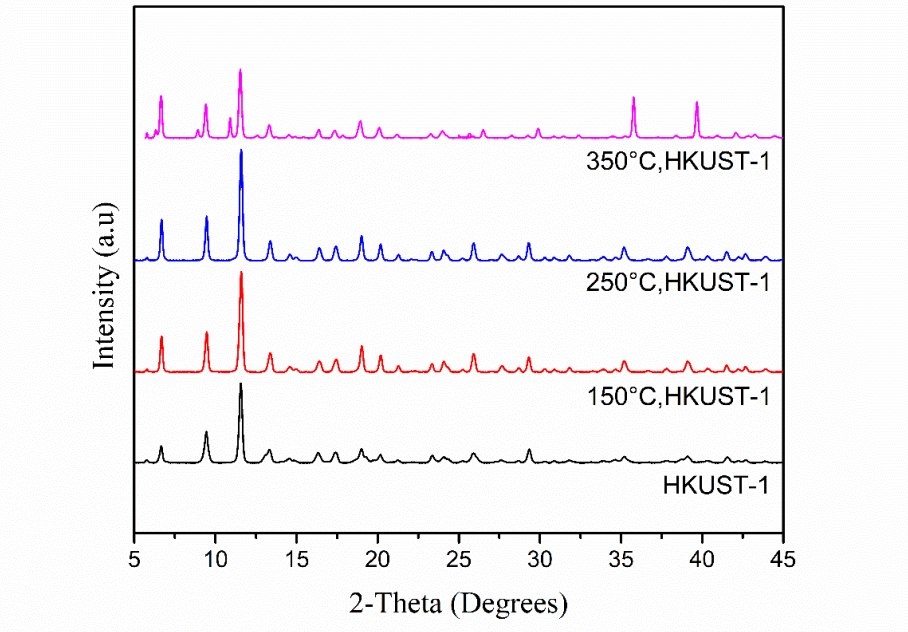

Figure 2 - 2: XRD spectrum of HKUST-1 sample produced at different $scCO_2$ injection temperatures. The sharp peaks at low 2Θ angles indicate the microporous structure of HKUST-1.

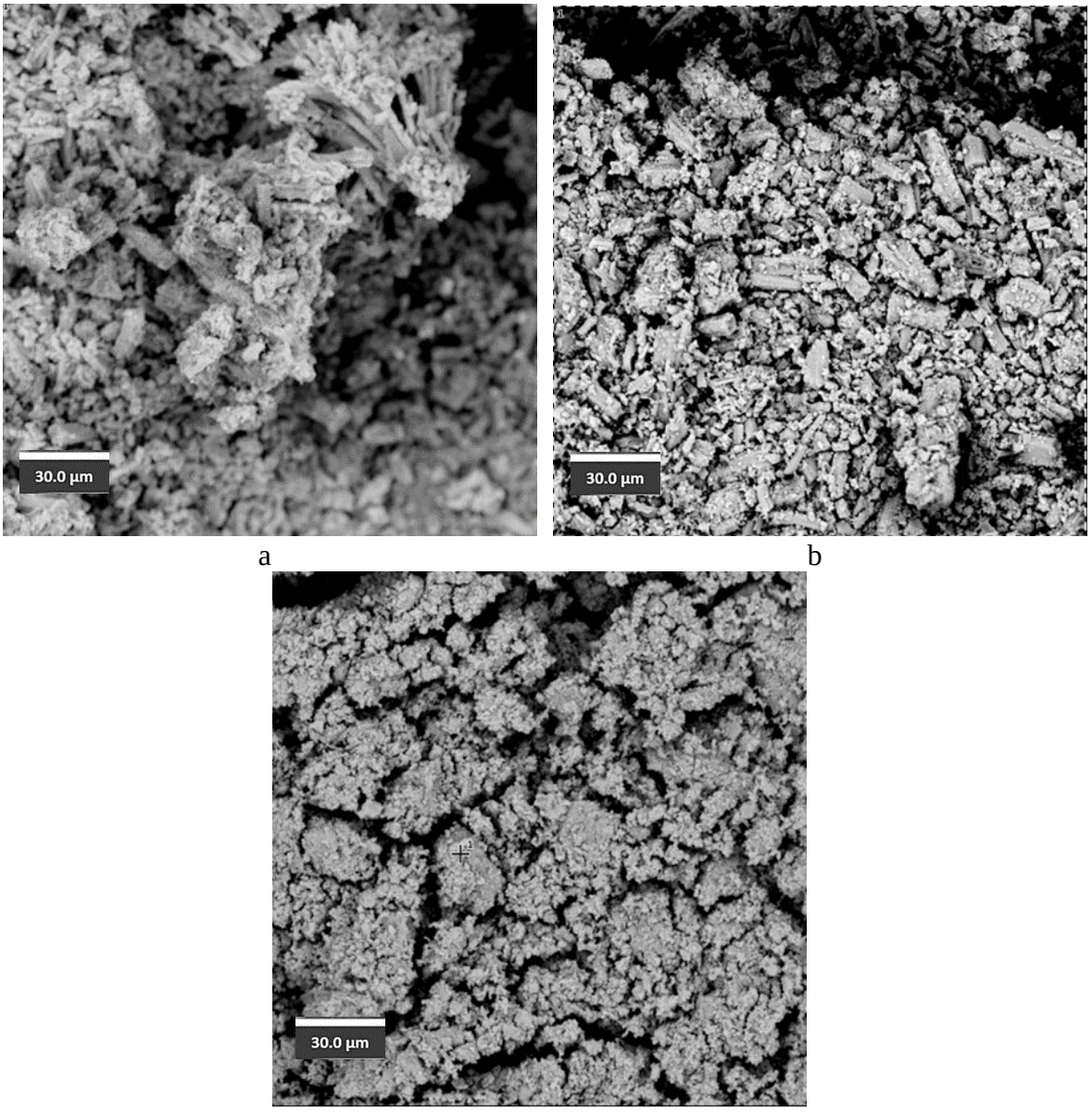

a b

c

Figure 2 - 3: SEM micrographs of HKUST-1 synthesized by a continuous flow $scCO_2$ reactor at varying synthesizing temperatures: (a) T_{inj} = 150 ºC, (b) T_{inj} = 250 ºC, (c) T_{inj} = 350 ºC.

The morphologies and microstructures of the HKUST-1 were studied using scanning electron microscopy (SEM). Figure 2 - 3 shows that, in general, higher temperature conditions yield smaller particle sizes and higher aspect ratios. At T_{inj} = 150 °C, see Figure 2 - 3 (a), MOFs are a mixture of octahedral and rod-like structures in the 2 – 15 µm range, consistent with previous reports. [67] Exposed to higher temperatures during synthesis, the individual structures tend to clump together, e.g., at T_{inj} = 250°C both rod-like particles and agglomerates are present, see Figure 2 - 3 (b), and T_{inj} = 350°C the sample consists primarily of fused aggregates, see Figure

2 - 3 (c). Similar observations were made by Pokhrel et al. [81, 82]; the authors also suggested that incorporating a functionalization group may be a promising strategy to prevent agglomeration.

The samples' specific surface area and porosity were determined by nitrogen adsorption-desorption measurements (Micromeritics ASAP 2020). Before measurement, the samples were activated under consistent conditions. The Barrett-Joyner-Halenda (BJH) method was used to calculate the pore sizes. Figure 2 - 4 (a) shows that the samples' BET surface areas range between 380 – 1528 $m^2 g^{-1}$. A strong correlation was observed between the surface area and the CO_2 injection temperature, with the maximum surface area at T_{inj} = 150 °C. As the synthesis temperature increases beyond that, the BET surface area decreases, which can be attributed to the formation of agglomerates and the decrease in the size of the crystallites, which in turn reduces the available surface area for gas adsorption. The presence of CuO (shown in PXRD, Figure 2 - 2 at higher synthesis temperatures indicates the MOF structures are damaged; additionally, the CuO could block the pores of the frameworks, reducing the specific surface area. These findings highlight the importance of understanding the mixing and temperature distribution in the reactor. Furthermore, a proper understanding of mixing and temperature distribution can minimize the formation of hot spots, which negatively impact the reaction efficiency and, in some cases, even lead to dangerous conditions such as thermal runaway. Conversely, inadequate mixing or uneven temperature distribution can result in incomplete reactions or even the formation of unwanted by-products, which can lead to waste and economic losses. Figure 2 - 4 b illustrates the relationship between the BJH pore radius and the synthesis temperature, exhibiting a similar trend to the BET surface area. At T_{inj} = 150 °C, the largest pore sizes are ~10.5 - 11.5 Å. The pore sizes are reduced to ~2 Å when fussed aggregates are formed at T_{inj} = 350 °C.

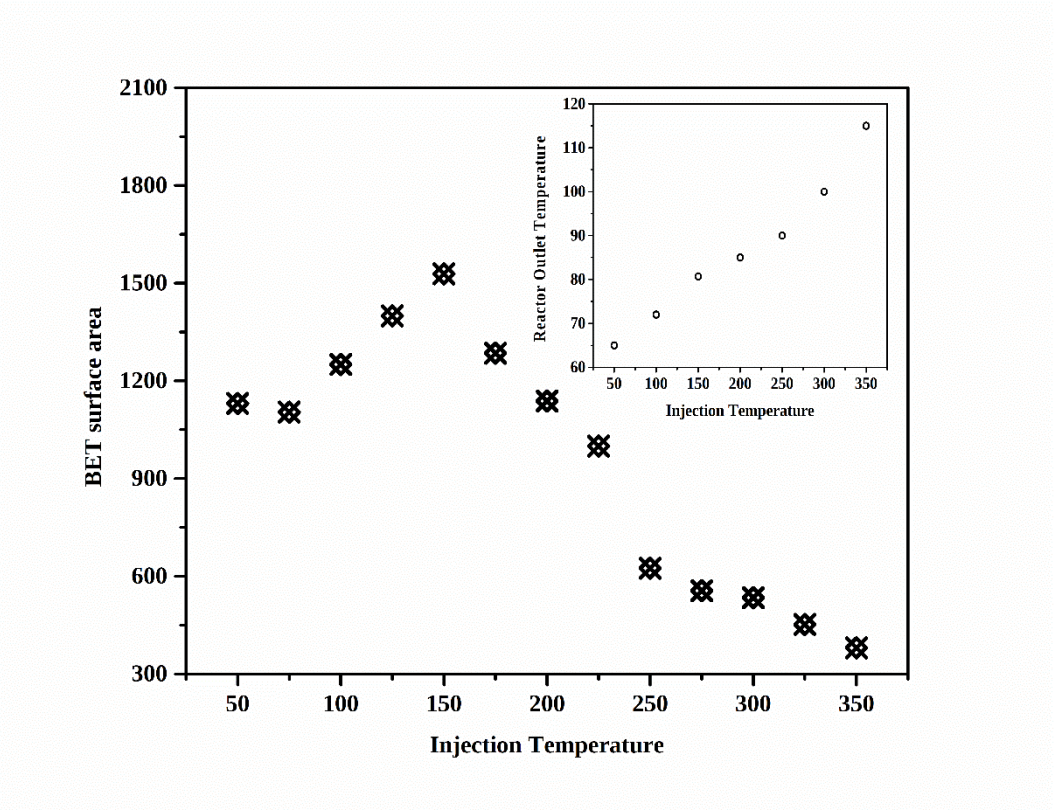

a

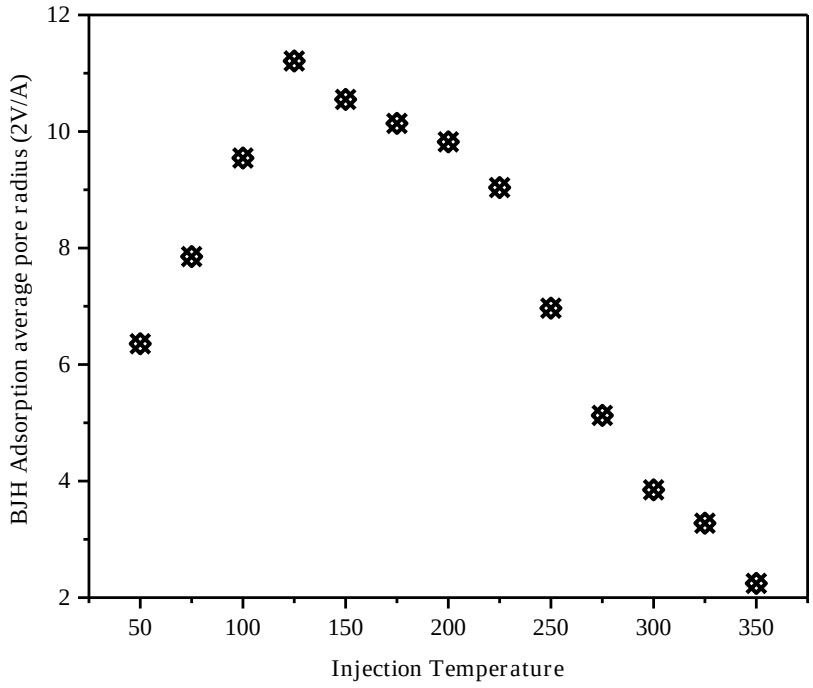

b

Figure 2 - 4: HKUST-1 Properties: a) BET surface area vs. scCO$_2$ injection temperature. b) BJH average pore radius vs. scCO$_2$ injection temperature

The thermal stability of HKUST-1 in a nitrogen environment is shown in

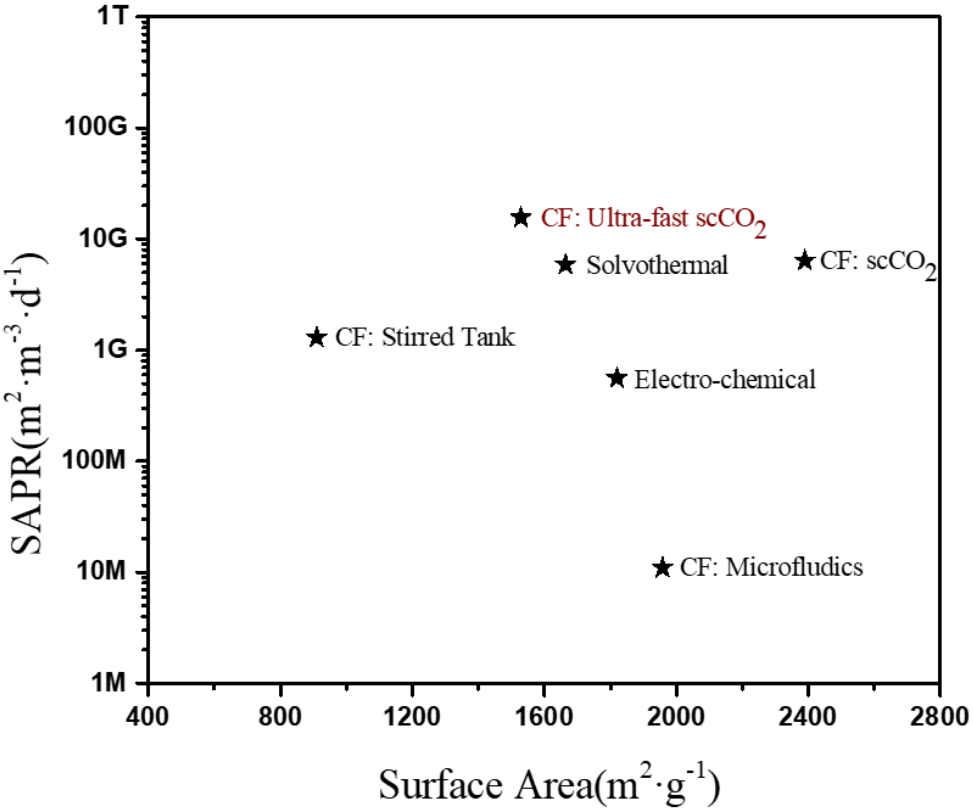

Figure 2 - 5 through TGA. The trends of all the samples are similar, showing changes in the quality of the samples over time. The TGA analysis reveals three distinct sample weight loss stages, which agree with previous reports. [83] In low-temperature regions (T < 200 °C), the reduction in the sample mass is due to the loss of water and other molecules through evaporation. The molecular formula of HKUST-1 MOF is assumed to be $Cu_3(BTC)_2(H_2O)_3$, with the number of crystal-bond water groups x ~ 3.0. In the T = 200 - 300°C range, the sample did not experience any significant mass change, confirming the framework's thermal stability at higher temperatures. A sharp decrease in weight (about 27.5 wt.%) at T ~ 340°C is caused by the decomposition of the BTC linker. It is worth mentioning that HKUST-1@150°C displayed slightly improved thermal stability compared to the other samples. This can be attributed to its superior crystal structure compared to the other samples.

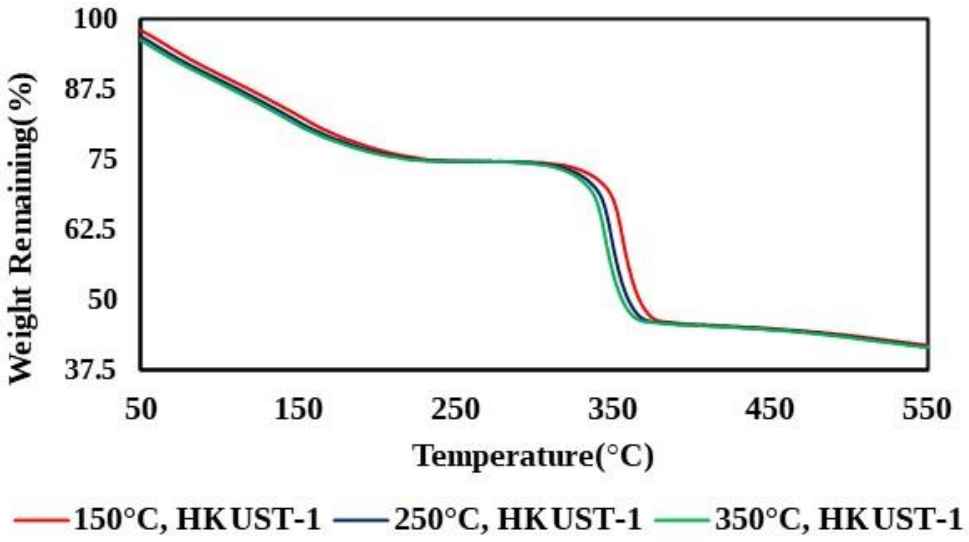

Figure 2 - 5: TGA curves of HKUST-1 synthesized at different temperatures. The HKUST-1 sample synthesized at 150°C displays improved thermal stability compared to the other samples, owing to its higher degree of crystallinity.

Comparing the efficacy of MOF synthesis methods can be challenging due to several factors, such as the compositions of precursors and varying molar ratios used across methods. Furthermore, the measurement techniques can impact the characterization of morphology parameters, including particle size, uniformity, and surface area. Historically, reaction time, space-time yield (STY), and surface area production rate (SAPR) have been employed to evaluate the scalability of synthesis analysis.[74, 75, 84] Though imperfect, these metrics offer a means to assess the relationship between the production rate and the material quality. Table 2 - 1 and Figure 2 - 6 compare both metrics for different synthesis methods. The current work shows the highest SAPR for (τ_{res} = ~650 ms); however, it came at the cost of a reduced BET surface area of 1528 $m^2 \cdot g^{-1}$, compared to the results reported by Rasmussen et al., who utilized a longer residence time $scCO_2$ reactor (τ_{res} =70 – 170 sec) and consistently reported BET surface area of over 2,000 $m^2 \cdot g^{-1}$ with highest BET surface area of 2,389 $m^2 \cdot g^{-1}$.

Table 2 - 1: HKUST-1 Properties: Comparison of synthesis methods of the HKUST-1 MOF, including surface area (SA) and SAPR.

Synthesis Method	SA	SAPR $m^2 \cdot m^{-3} \cdot d^{-1}$
Solvothermal batch [85]	BET 692.2	N/A
Continuous flow –Stirred Tank[84]	Langmuir 910	$1.3*10^9$
Continuous flow - Microwave[84]	Langmuir 600	$2.4*10^{11}$
Continuous flow - Microfluidics[86]	BET 1,958	$1.1*10^7$
Continuous flow - solvothermal[30]	1,805	$2.5*10^{10}$
Continuous flow - Hydrothermal[68]	BET 1,950	N/A
Continuous flow -$scCO_2$[73]	BET 2,389	$6.4*10^9$
Electrochemical[12]	Langmuir 1,820	$5.6*10^8$
This work	**BET 1528**	**$7.93*10^{11}$**

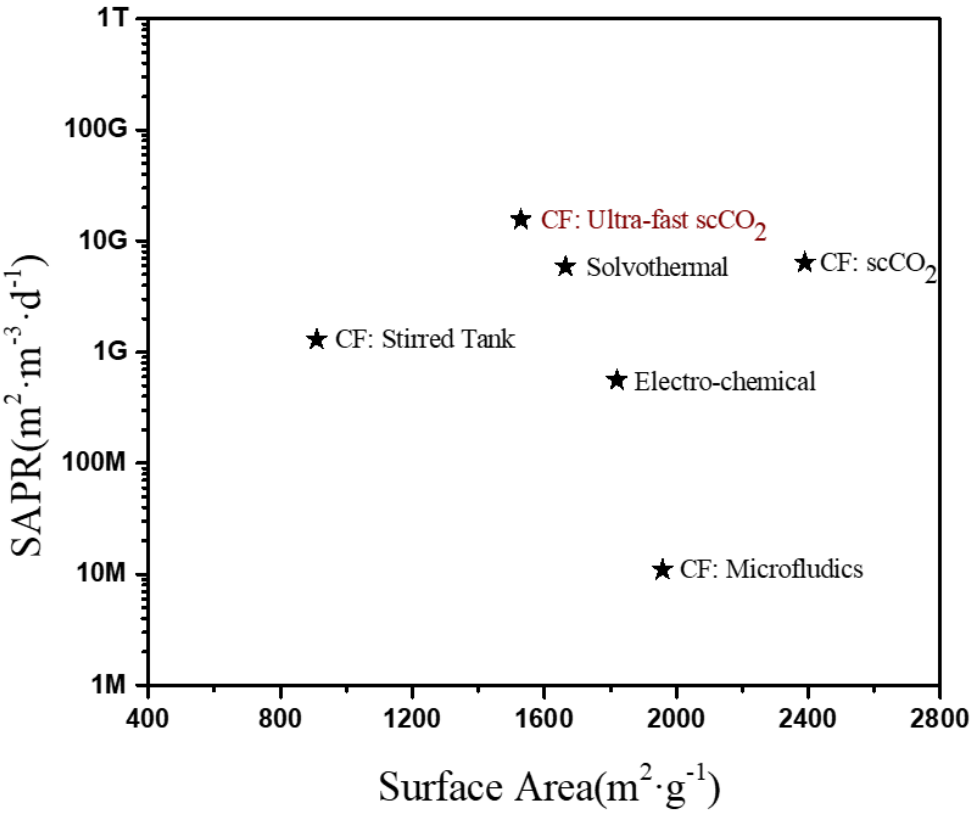

Figure 2 - 6: HKUST-1 Properties: SAPR vs. SA plot.

2.4 Conclusions

In summary, we reported a study focused on identifying the properties of HKUST-1 based on the synthesis condition. Previously Rasmussen et al. showed that in the constant temperature $scCO_2$ reactor with a residence time of ~ 100 sec, the properties of synthesized HKUST-1 did not vary significantly once the $scCO_2$ conditions for the mixture were met. [73] In a reactor with a shorter residence time, the temperature non-uniformity in the reactor is inevitable. It is the result of mixing room temperature reagents and the hotter $scCO_2$. Before complete mixing occurs, the reagents could be exposed to $scCO_2$ injection temperature (T_{inj} = 50°C - 350°C), causing partial degradation of the MOFs.

$ScCO_2$ injection enables a rapid (~650 ms) single-step synthesis of high-quality HKUST-1 MOFs by a continuous flow process. The defined operational envelope of the synthesis process can be readily controlled by varying the flow rates and temperatures of the CO_2 injection. The high reactor throughput and high quality of synthesized MOF could lead to scale-up MOF production in $scCO_2$ for multiple applications.

Chapter 3 Nano-Composite Synthesis: Harnessing the Potential of Continuous Flow scCO$_2$ Reactor for Sub-Second synthesis of GO@HKUST-1.

3.1 Introduction

The development of MOFs represents a significant advancement in crystalline microporous solids. These unique materials are constructed by assembling metal ions or clusters in conjunction with organic ligands, resulting in a periodic framework. [87, 88] The resulting structures possess a rigid three-dimensional topology and a high internal surface area, rendering them highly attractive for various applications. These include, but are not limited to, gas storage [89], gas purification [90-92], heterogeneous catalysis [93, 94], and chemical sensing. [95, 96]

Recent advancements in the field of MOFs related research have led to the development of MOF composites characterized by embedding nanoscale particles within conventional microporous skeletons. [97] As a result, MOF composites can incorporate functional species, such as nanoscale metal particles or oxides, confined within the microporous networks. [98, 99] Recent research has focused on developing metal-organic framework (MOF) composites utilizing materials such as GO [100, 101], Fe_3O_4 [102-104], ZnO [105, 106], precious metal nanoparticles [107-109], and alumina or silica. [110-113]

Studies have demonstrated the potential of incorporating GO into MOFs to enhance their adsorption capabilities. Bandosz et al. [114] presented two GO@MOFs nanocomposites, MOF - 5/GO and HKUST - 1/GO, which exhibited similar crystalline structure and porosity as the parent MOFs, but with higher ammonia adsorption capacity due to the creation of new pores between the MOF units and GO. Recently, new GO@MOFs nanocomposites were synthesized and found to possess higher adsorption capacity than their parent MOFs, indicating the potential of this approach for developing advanced adsorbents. Zhou et al. [115] presented

a GrO@MIL-101 composite with a CO_2 adsorption capacity of 3.6 mmol/g (T = 298 K, P = 1 bar), significantly higher than that of MIL-101 (1.6 mmol/g). Ram et al. [116] developed a simple method to prepare hybrid GO@ZIF-8 nanocomposites, with the composite (ZG - 20) displaying remarkable CO_2 storage capacity (72 wt%) in comparison to the parent ZIF – 8 (27.2 wt%). Liu et al. [117] synthesized composites using Cu - BTC and graphene layers and found that the resulting materials exhibited an approximately 30% increase in CO_2 storage capacity, from 6.39 mmol/g of Cu - BTC to 8.26 mmol/g of CG - 9 at 273 K and 1 atm. GO@HKUST-1 nanocomposite also exhibits enhanced hydrogen absorption properties. This is due to the synergistic effect of combining the high surface area and porosity of MOFs with the high chemical stability of GO.

The synthesis of GO@HKUST-1 nanocomposites typically involves using the conventional solvothermal method. [85] In this method, preparing HKUST-1 involves heating the solution to 180 °C to form crystalline $Cu_3(BTC)_2$. However, this process is time-consuming, as the $Cu_3(BTC)_2$ must be kept in an autoclave for a prolonged period, varying from 1 day to a few weeks. [67] Despite this, the solvothermal method is still widely used due to its tunable reaction conditions and the ability to control the nucleation rate and crystal growth by controlling the concentration and temperature gradient. [118-121] Other methods for the rapid preparation of HKUST-1 include microwave heating, ultrasound irradiation, mechanochemistry, and solvothermal synthesis, summarized in Table 3- 3. [122-125] The conventional solvothermal and electrochemical methods tend to have a longer synthesis time to yield MOFs with high surface areas. On the other hand, methods such as mechanochemistry, microwave heating, and ultrasound irradiation can reduce the synthesis time. Still, they do not necessarily yield MOFs with high surface areas (> 1000 m^2/g), making them less suitable for large-scale production. Moreover, their synthesis often requires multiple steps, increasing preparation time and costs [125]. As a result, there is a growing need for efficient and cost-effective synthesis

methods, such as continuous flow synthesis, to facilitate the production of MOF-related nanocomposites. [49, 73] This need for efficient and cost-effective synthesis methods is particularly pressing in the large-scale production of MOF-related nanocomposites for applications such as gas separation and heterogeneous catalysis, where the ability to produce these materials in large quantities is crucial.

This chapter describes a method for synthesizing GO@HKUST-1 nanocomposites that is both fast and efficient. Our efforts were focused on optimizing the synthesis process of the nanocomposites to produce particles with high surface area and high yield.

3.2 Experimental Methods

3.2.1 Chemicals

Copper nitrate trihydrate ($Cu(NO_3)_2.3H_2O$,99.99%) and benzene - 1,3,5 - tricarboxylic acid (BTC, 95%) were purchased from Sigma-Aldrich and used as received. Per the reported procedures, the precursor material was meticulously prepared, utilizing 99% anhydrous ethanol as a solvent. [73] Multilayer turbostratic reactive GO with a 90% or higher purity was sourced from Hydrograph Inc and used to synthesize the GO@HKUST-1 composite material. Ultra-pure grade Nitrogen (N_2) and Carbon dioxide (CO_2) gases were procured from Praxair with purities of 99.9995%.

3.2.2 Reactor Design

The reactor design is documented in section 2.2.1 and briefly explained here. The flow diagram of the reactor is shown in Figure 2 - 1. The continuous-flow $scCO_2$ reactor is designed to function in a temperature range of T = 298–873 K (25 – 600 °C) and a pressure range of P = 0.10 – 30 MPa. The synthesis process involves combining two precursor streams, namely metal and organic precursors, without heating, along with heated $scCO_2$ in the counterflow mixing section to mix and heat the reactants rapidly. Upon leaving the counterflow reactor

section, the effluent rapidly cools to room temperature and passes through a pressure regulator. The reaction products are maintained in the liquid phase while the CO_2 is discharged into the fume hood through natural aspiration.

3.2.3 Synthesis of GO@HKUST-1 and HKUST-1

The synthesis of HKUST-1 was conducted as previously described in Chapter 2. The GO@HKUST-1 composite material was synthesized by incorporating 5 wt% GO in situ during the synthesis of HKUST-1, along with the organic precursor materials. The concentration of the precursor was held constant. The particles were collected and isolated through centrifugation (9,000 rpm for 10 minutes) using an Allegra X – 30 centrifuge (Bechman Coulter). The particles were subsequently washed twice with ethanol. The blue product was transferred to glass vials and dried at 393 K overnight. The final yield of the product was determined using an analytical balance (ME54TE, Mettler Toledo).

3.2.4 General Characterizations

The X-ray diffraction (XRD) spectra were obtained using a D8 Advance (Bruker) equipped with an IμS 1 - D detector. The instrument was operated under the following conditions: 40 kV, 40 mA for CuKα (λ = 1.5418 Å) radiation at room temperature, over an angular range of 2θ = 0° - 60°, and at a scanning rate of 2 deg·min^{-1}. Fourier Transform Infrared (FTIR) spectra were obtained at ambient temperature using a NICOLET iS10 - FTIR spectrometer from Thermo Scientific. Thermogravimetric analysis (TGA) was carried out using a TA Instruments Thermobalance Q500 HR under a nitrogen atmosphere. The instrument was operated in Hi–Res mode, with a maximum heating rate of 5 K min^{-1} (sensitivity 1, resolution 5), from room temperature to 873 K. The morphology of the activated sample was analyzed using an FEI Sirion XL30 scanning electron microscope (SEM) operating at an acceleration voltage of 15 kV. To prepare the sample for the SEM imaging, 15 mg of the activated material was dispersed on carbon tape and sputter-coated with gold using a Manual

Sputter Coater (Ted Pella) to minimize charging effects. The technique of physisorption analysis was employed by transferring 150 mg of the activated sample to a pre-weighted sample tube. The sample was degassed at 383K using a Smart VacPrep 067 (Micrometrics) until the outgassing rate was less than 5 µm Hg. The sample tube was re-weighed to ensure a consistent mass for the degassed sample. Nitrogen (N_2) isotherms were obtained at 77 K using a liquid nitrogen bath (3Flex, Micrometrics) with ultra-high-purity grade Nitrogen gas (99.999% purity) sourced from Praxair. The Renishaw inVia instrument, which had a Leica microscope built in, was used for Raman spectroscopy. The samples were excited using the 532 nm Ar line, and the spectral resolution was approximately 4 cm^{-1}. The acquisition of each spectrum involved taking 10 accumulations of 10 seconds each.

3.2.5 Experimental Conditions

A series of five experiments were performed to investigate the impact of synthesis temperature on the crystallinity, physisorption, and morphology of GO@HKUST-1. The $scCO_2$ injection temperature was varied between T_{inj} = 150 – 350 °C to identify the favorable conditions for GO@HKUST-1 nano MOF composite synthesis. Throughout all experiments, the reactor pressure was fixed at P = 10 MPa, while the flow rates of the precursor pumps (Pump 1 and Pump 2) and $scCO_2$ flow rate (Pump 3) remained consistent at 10 mL min^{-1}, 10 mL min^{-1}, and 25 mL min^{-1}, respectively.

3.3 Results & discussion

The X-ray diffraction patterns for HKUST-1 and GO@HKUST-1 are depicted in Figure 3- 1. The diffraction pattern of HKUST-1, as represented by its well-defined characteristic peaks, demonstrates the crystalline nature of the material. [9, 100, 114] A GO peak typically located at $2\theta = 9.29°$ [114] is not visible due to the overlap with HKUST-1 spectra. The diffraction patterns for GO@HKUST-1 composites reveal that the structure of the parent MOF is preserved, as evidenced by the absence of any significant changes in the peak positions. The

diffraction peak intensities increased with the addition of GO. The high intensity observed for GO@HKUST-1 could be attributed to a higher degree of MOF crystallization. The characteristic GO peak at $2\theta = 9.29°$ is absent in the XRD patterns of GO@HKUST-1 composites, possibly because the GO may have been completely exfoliated during the growth of the crystals. This suggests that the presence of GO does not impede the linkage among the organic bridges and copper clusters in the M. However, additional analysis is needed to gain insight into the crystal synthesis mechanism. The XRD pattern of GO@HKUST-1 synthesized at $T_{inj} = 250$ °C exhibits the highest diffraction peak intensity, indicating that it has the best crystallinity. This also suggests that at the synthesis condition of $T_{inj} = 250$ °C, 5 wt% GO doping can produce MOF crystals with a uniform shape, as supported by previous research on HKUST-1 doped with small amounts of GO. [82] However, studies have shown that when excessive amounts of GO are added, the GO inclusions may act as a physical barrier that hinders crystal growth. [126] Additional experiments and analysis are needed to understand the composites' structure.

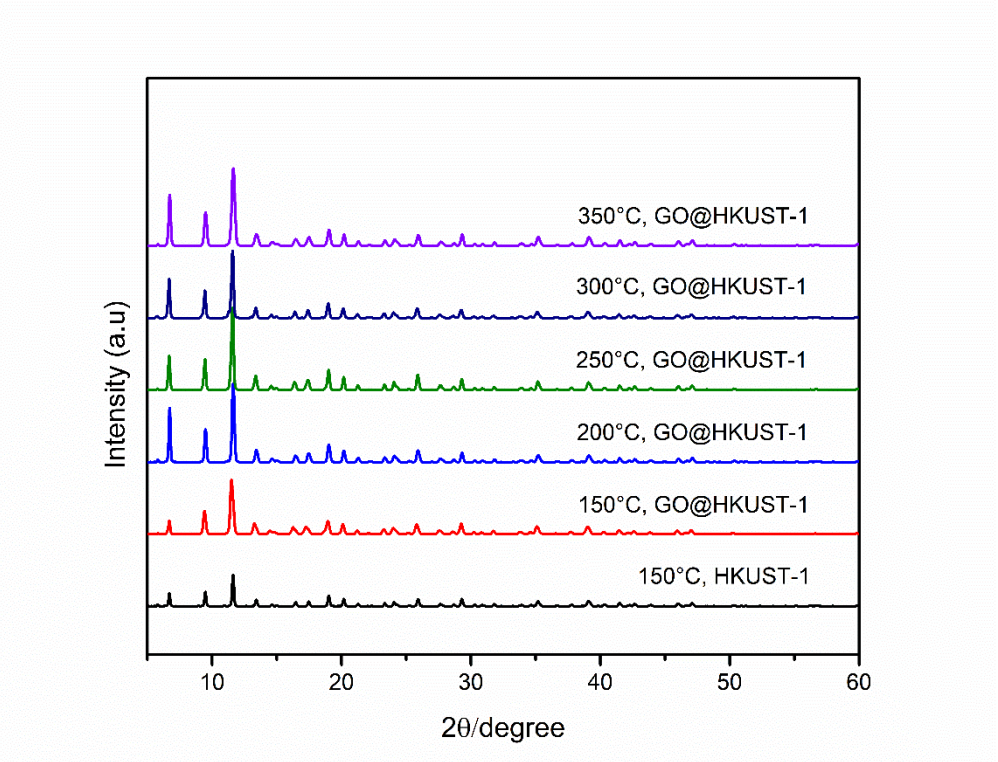

Figure 3- 1. XRD spectrum of GO@HKUST-1 sample produced at different $scCO_2$ injection temperatures. The sharp peaks at small 2Θ angles indicate the microporous structure of GO@HKUST-1.

The composite material can be examined by SEM images, shown in Figure 3-2. SEM images of HKUST-1 are also included for comparison. Figure 3-2 (a) depicts the crystals of HKUST- 1 synthesized at T_{inj} = 150 °C. They have non-uniform shapes consisting of octahedral and rod-like structures, as expected from previous studies[67], with varying crystal sizes ranging from 2 - 15 μm. Figure 3-2 (b) - (f) illustrates the GO@HKUST-1 composite. The images show that the GO layer is present on the surface of the HKUST-1.

In Figure 3-2 (b, c), lower temperature synthesis yields a fraction of the GO@HKUST-1 particles appearing as rod-like crystals. The T_{inj} = > 250 °C case has better crystallization -- the resulting composite has octahedral crystals. Additionally, there are apparent cracks and defects on the surface of octahedral crystals. Possibly due to the GO layer acting as a barrier for crystal growth. A similar observation has been reported by Pan et al. [71, 105]

Figure 3-2 (b-f) demonstrates that the small HKUST-1 particles co-exist within the GO layers. The SEM images of the composite show that GO covers HKUST-1 particles. We performed the particle size measurements using Images J software [127], widely used for analyzing particle sizes, e.g., refs [128] [129]. The particle sizes in the GO@HKUST-1 synthesis are ~ 16 ± 4 μm and are more uniform than in HKUST-1 without GO. Previously Pan et al. [71, 105] suggested that the presence of GO in batch synthesis adds constraints to the growth of HKUST-1 crystals, thus resulting in smaller crystals size. In other words, the presence of GO during the growth of HKUST-1 crystals may cause distortion force on the crystals, leading to a reduction of the crystal size and the formation of cracks. The GO flakes act as a support and barrier, preventing the MOF crystallites from forming large, non-uniform particles.[130] This hypothesis needs further testing for the scCO2 continuous flow system as the time scale for nucleation, and the crystal growth are significantly faster than in the batch process.

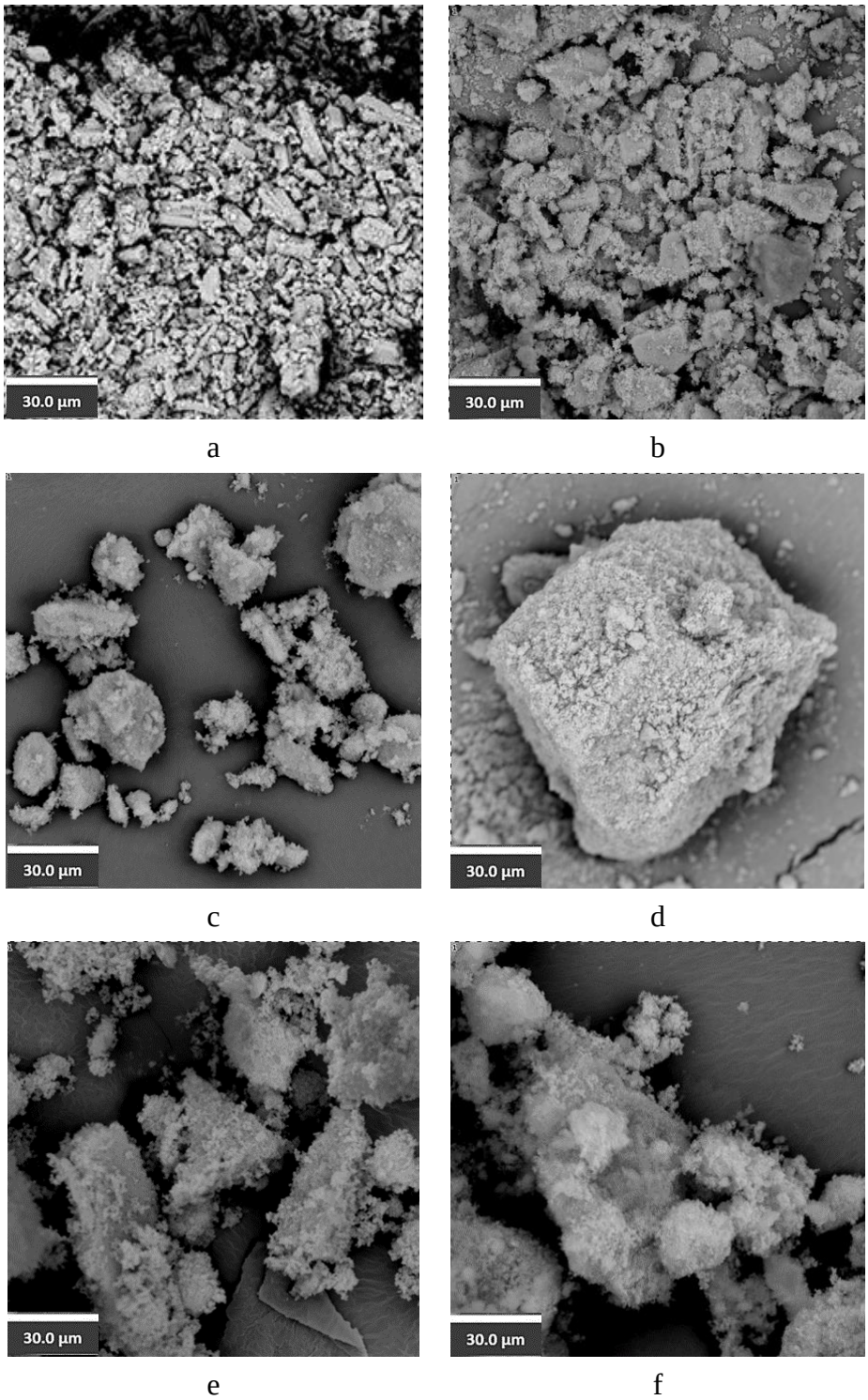

Figure 3-2: SEM micrograph of HKUST-1 and GO@HKUST-1 synthesized by a continuous flow $scCO_2$ reactor at varying injection temperatures (T_{inj}): a) HKUST-1 synthesized at T_{inj} = 150 ºC, GO@HKUST - 1 synthesized at b) T_{inj} = 150 ºC, c) T_{inj} = 200 ºC, d) T_{inj} = 250 ºC, e) T_{inj} = 300 ºC f) T_{inj} = 350 ºC.

Figure 3- 3 illustrates the elemental mapping for the GO@HKUST-1 (T_{inj} = 250 ºC) particles. The elemental mapping images reveal a uniform distribution of Cu from the MOF crystals and an increased C concentration due to the presence of GO on the surface.

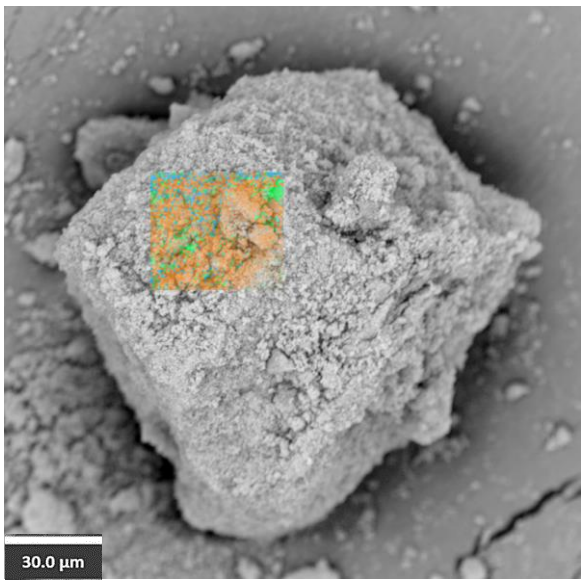

Figure 3- 3: EDS mapping of GO@HKUST-1 synthesized at T_{inj} = 250 ºC

Table 3- 1 and Table 3- 2 display the results of the elemental analysis conducted on the HKUST-1 and GO@HKUST-1. The increase in carbon content in the composite samples compared to their parent samples provides further confirmation of the presence of GO. The elemental analysis of GO@HKUST-1 reveals that carbon is the most abundant element (58.53 atomic %), followed by oxygen (31.27 atomic %) and nitrogen (8.62 atomic %). Although copper's atomic concentration is relatively low (15.25 atomic %), its weight percentage in the compound is significant (25.64 wt. %). This observation suggests that copper atoms in HKUST-1 significantly contribute to the material's overall mass. The elemental analysis provides valuable insights into the composition of GO@HKUST-1 and emphasizes the significance of considering both atomic and weight concentrations while characterizing composite materials.

Table 3- 1: Weight concentration-based elemental analysis

Sample	% Carbon	%Copper	%Hydrogen	%Nitrogen	%Oxygen
150°C, HKUST-1	51.10	16.42	6.07	11.10	34.57
250°C, GO@HKUST-1	58.53	15.25	4.06	8.62	31.27

Table 3- 2: Atomic concentration-based elemental analysis

Sample	% Carbon	%Copper	%Hydrogen	%Nitrogen	%Oxygen
150°C, HKUST-1	36.54	29.30	6.06	10.91	30.07
250°C, GO@HKUST-1	39.85	25.64	3.99	9.95	30.96

Figure **3-4** shows the FTIR spectra of HKUST - 1 and GO@HKUST - 1. The spectra are similar, with the prominent characteristic peak aligning with the published FTIR spectrum of HKUST - 1. [131] The bands detected at 1645 $cm^{-1,}$ and 1590 cm^{-1} in both HKUST - 1 and GO@HKUST - 1 are attributed to the asymmetric stretching vibrations of the carboxylate groups present in BTC. Symmetric stretching of the same groups is observed at 1450 cm^{-1} and 1370 cm^{-1}. Moreover, the 1300 − 600 cm^{-1} region displays multiple bands linked to the out-of-plane vibrations of BTC. The unoxidized sp^2 bonds result in C = C peaks at the 1590 – 1620 cm^{-1} range, C - O vibrations at 1250 cm^{-1}, and C - O stretching vibrations within the 1720 - 1740 cm^{-1} range, suggesting the presence of various oxygen-containing functional groups in the GO structure. The band at 1111 cm^{-1} is related to the tensile vibration of the C – O – Cu bond. Notably, the observation of all characteristic peaks in GO@HKUST-1 indicates that the structural integrity of HKUST-1 has been preserved. It is worth noting that the composites exhibit a higher peak intensity than that of HKUST-1, which is consistent with the XRD experiment findings.

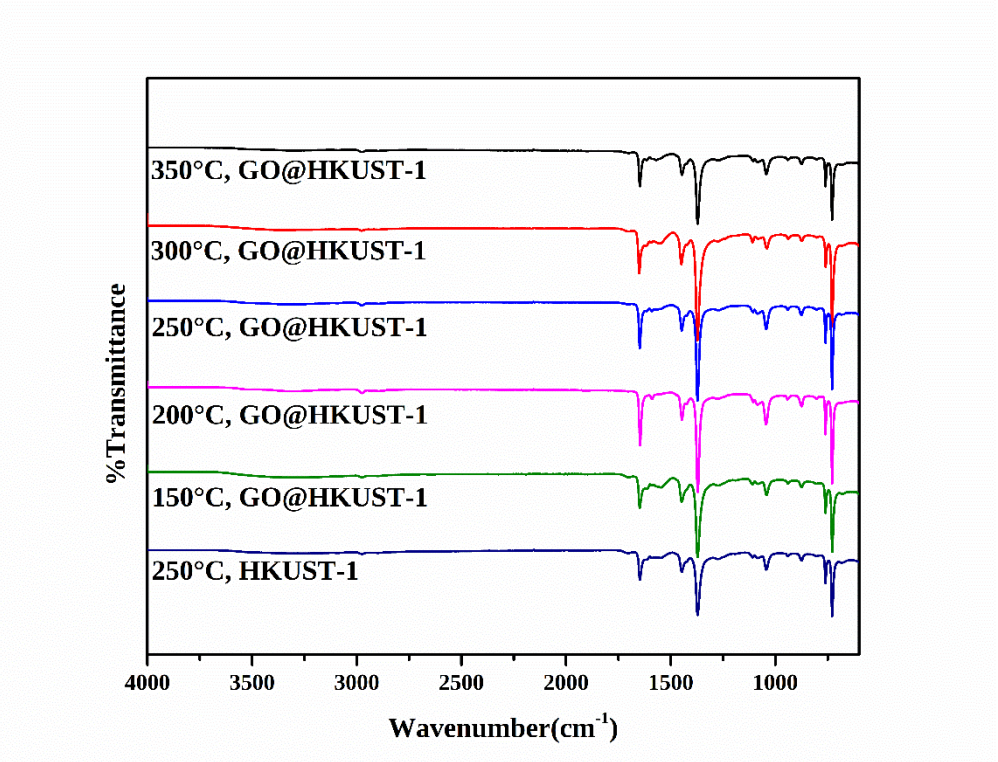

Figure 3-4: FTIR spectra of HKUST-1 and GO@HKUST-1.

Figure 3-5 shows the Raman spectra of HKUST-1 and GO@HKUST-1. The Raman spectra of GO@HKUST-1 samples have been studied to obtain structural information on the hybrid material. Raman spectroscopy provides information on the vibrational modes of chemical bonds in materials, including GO and MOFs. The spectra reveal changes in the vibrational modes of the carbon and metal-organic framework components upon interaction. The Raman spectrum of HKUST-1@GO typically consists of several peaks in the range of 500 - 1800 cm^{-1}. The characteristic peaks in the spectra correspond to the stretching and bending vibrations of various chemical bonds, such as C-C, C-O, C=O, Cu-N, and Cu-O. The peak at around 1500 cm^{-1} is attributed to the stretching vibration of the C=C bonds in GO, indicating the presence of graphene oxide. The peak at around 1600 cm^{-1} corresponds to the stretching vibration of the BTC linkers' carboxylate (COO-) groups, indicating the MOF's presence. The symmetric stretching vibration of the CH_2 group of GO corresponds to the stretching and contracting of the CH_2 bonds in the graphene oxide structure, resulting in a

characteristic Raman peak at around 2800 cm^{-1}. This peak is particularly useful for identifying the presence of GO in a sample, as it is a strong and distinct peak that is not commonly found in other materials. Additionally, the intensity of the peak can provide information on the concentration and purity of GO in the sample. Changes in the intensity or position of these peaks can indicate changes in the material's structure or composition, such as the formation of new bonds or changes in bond angles.

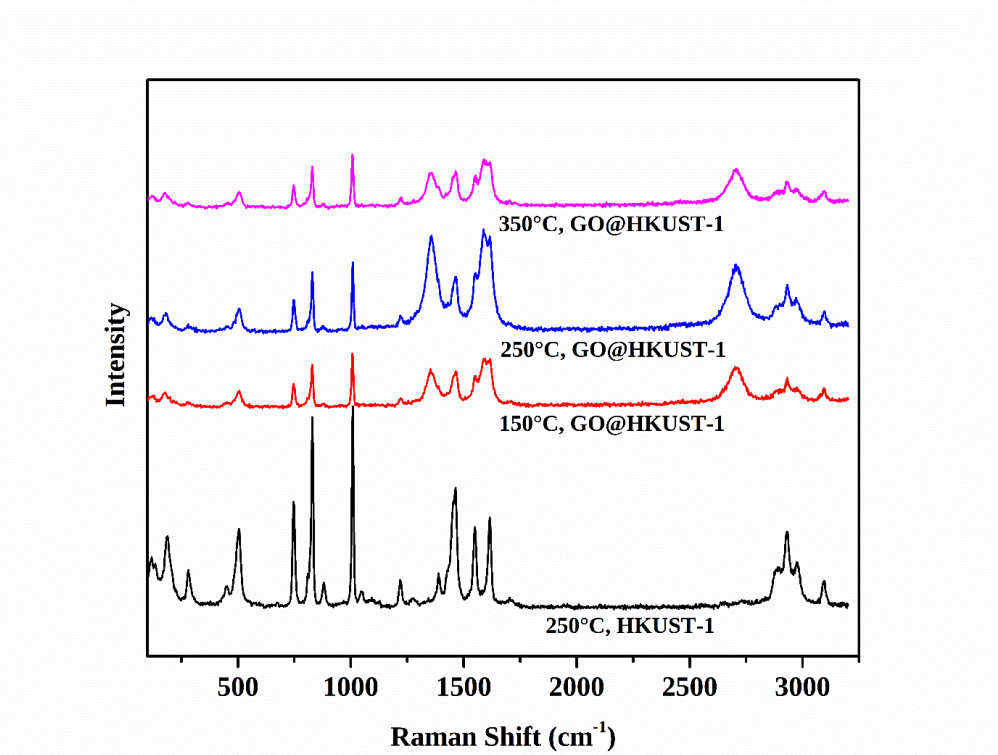

Figure 3-5: Raman spectra of HKUST-1 and GO@HKUST-1.

Figure 3-6 illustrates the thermal stability of HKUST-1 and GO@HKUST-1 in a nitrogen environment. The TG curves depict the changes in the sample quality over time. The trend of GO@HKUST-1 is similar to that of HKUST-1. Additionally, the TGA analysis reveals three weight loss stages for the HKUST-1 and GO@HKUST-1 samples, which align with those reported in the literature. [83] The first weight loss in the TG curves of HKUST-1 and GO@HKUST-1 samples at a temperature below ~ 175 °C results from the removal of guest molecules, which are the trapped molecules in the pores of the MOF structure. The second

weight loss between 175 °C and 325 °C corresponds to the removal of bound water, which refers to the water molecules that are physically adsorbed or chemically adsorbed on the surface of the MOF structure. The third weight loss, which starts at ~325 °C, corresponds to the decomposition of the MOF structure. This means that the MOF structure begins to break down, and the chemical bonds that hold the structure together weaken, resulting in a mass loss. The weight loss curve shows that adding GO significantly improves the thermal stability of HKUST-1. Among the synthesized composites, GO@HKUST-1 synthesized at 250ºC exhibits the best thermal stability, while GO@HKUST-1 synthesized at 350ºC shows the worst thermal stability. To quantify the structural degradation occurring at ~ 40ºC higher temperature for GO@HKUST-1 synthesized at 250ºC compared to GO@HKUST-1 synthesized at 350ºC. This can be explained by the higher degree of crystallization in the GO@HKUST-1 synthesized at 250 ºC. High crystallization can cause a decrease in the amount of material that is lost during thermal analysis. [132, 133] This is because crystalline materials typically have stronger bonds as they are more tightly packed and, thus, more thermally stable than amorphous materials. As a result, the onset of weight loss during a TGA experiment may be shifted to a higher temperature. The overall weight loss may be less for a highly crystalline sample than for a less crystalline or amorphous sample. It has been reported that bare GO decomposes at around 210 °C [130]; however, the weight loss due to GO is not significant for our nanocomposites mainly because of its relatively low content compared to the MOF.

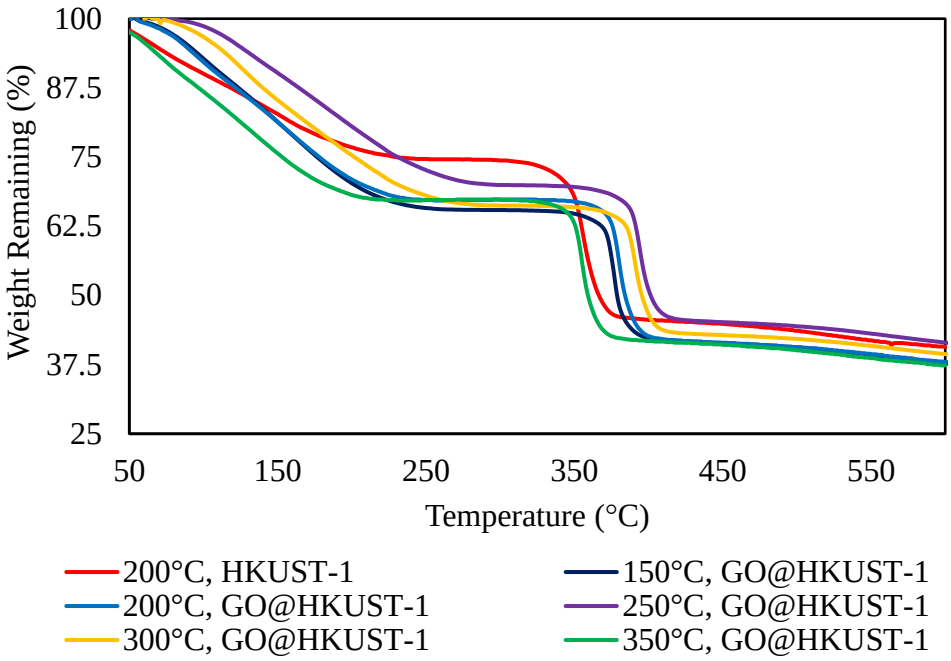

Figure 3-6: TGA curves of HKUST-1 and GO@HKUST-1 synthesized at different injection temperatures. The GO@HKUST-1 sample synthesized at 250°C displays improved thermal stability compared to the other samples, owing to its higher degree of crystallinity.

Five experiments were conducted to investigate the impact of $scCO_2$ injection temperature on the physisorption of GO@HKUST-1. The injection temperatures were set to 150 °C, 200 °C, 250 °C, 300 °C, and 350 °C to evaluate the temperature range within which MOFs can be formed while avoiding the degradation of GO@HKUST-1 MOFs to Cu_2O. Throughout the experiments, the reactor was maintained at a constant pressure of P = 10 MPa, while the flow rates of the precursor pumps, Pump 1 and Pump 2, as well as the $scCO_2$ flow rate (Pump 3), remained constant at 10 $mL \cdot min^{-1}$, 10 $mL \cdot min^{-1}$, and 25 $mL \cdot min^{-1}$, respectively.

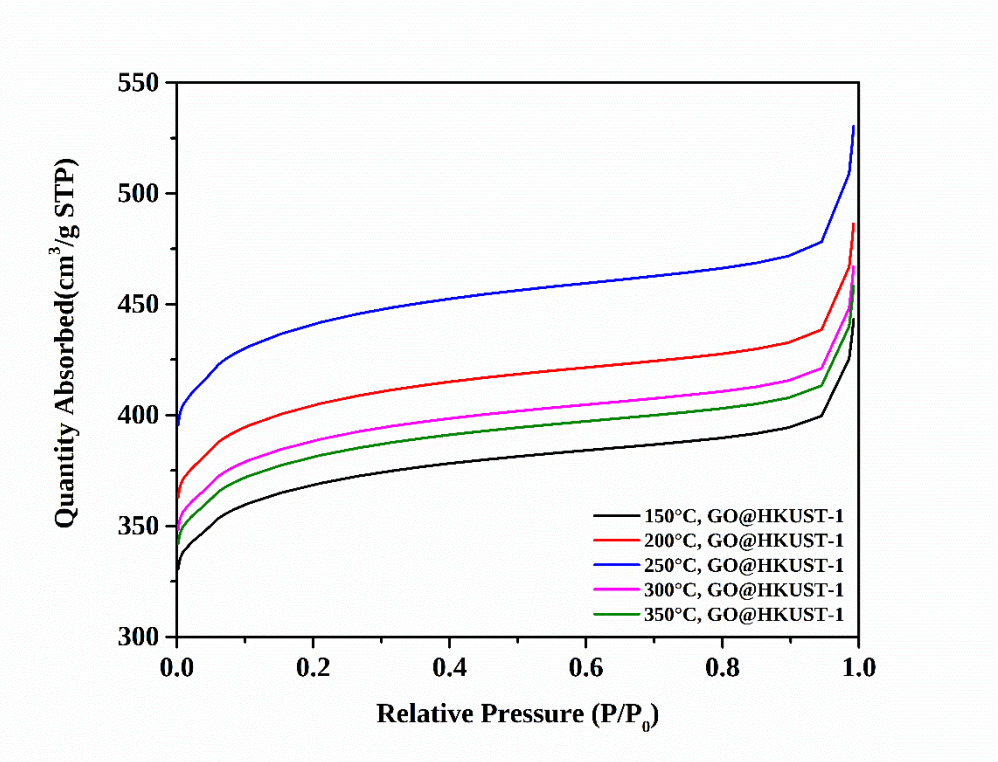

Figure 3-7: Nitrogen adsorption isotherms of the synthesized GO@HKUST-1.

To determine the surface area and porosity of the samples, N_2 adsorption-desorption experiments were conducted at 77 K, see Figure 3-7. The N_2 isotherms exhibited a typical type-I sorption behavior, characterized by a sharp increase at low nitrogen relative pressure, followed by a plateau, indicating that the samples possess abundant micro-pores. In addition, small type IV hysteresis loops were observed on the GO@HKUST-1 composites, suggesting the presence of narrow slit-like pores between HKUST-1 particles and GO layers, similar to other reports of MOF-GO composites. The N_2 isotherms of the GO@HKUST-1 composites showed higher adsorption capacity than HKUST-1, indicating that the former has a higher specific surface area. However, at T_{inj} = 150°C, the BET surface area of GO@HKUST-1 was 1171 $m^2 g^{-1}$, which is lower than that of the parent MOF, HKUST - 1. The decrease in surface area was ascribed to the surplus of unreacted GO, which possesses a considerably lower surface area than the HKUST-1 MOF. However, at higher injection temperatures (T_{inj} > 200 °C), the BET surface area of GO@HKUST-1 was higher than that of the parent MOF, indicating better

thermal stability of GO@HKUST-1 at higher temperatures. Nonetheless, adding GO is expected to induce enhanced microporosity in the HKUST-1, leading to improved adsorption and faster sorption kinetics than pure HKUST-1.

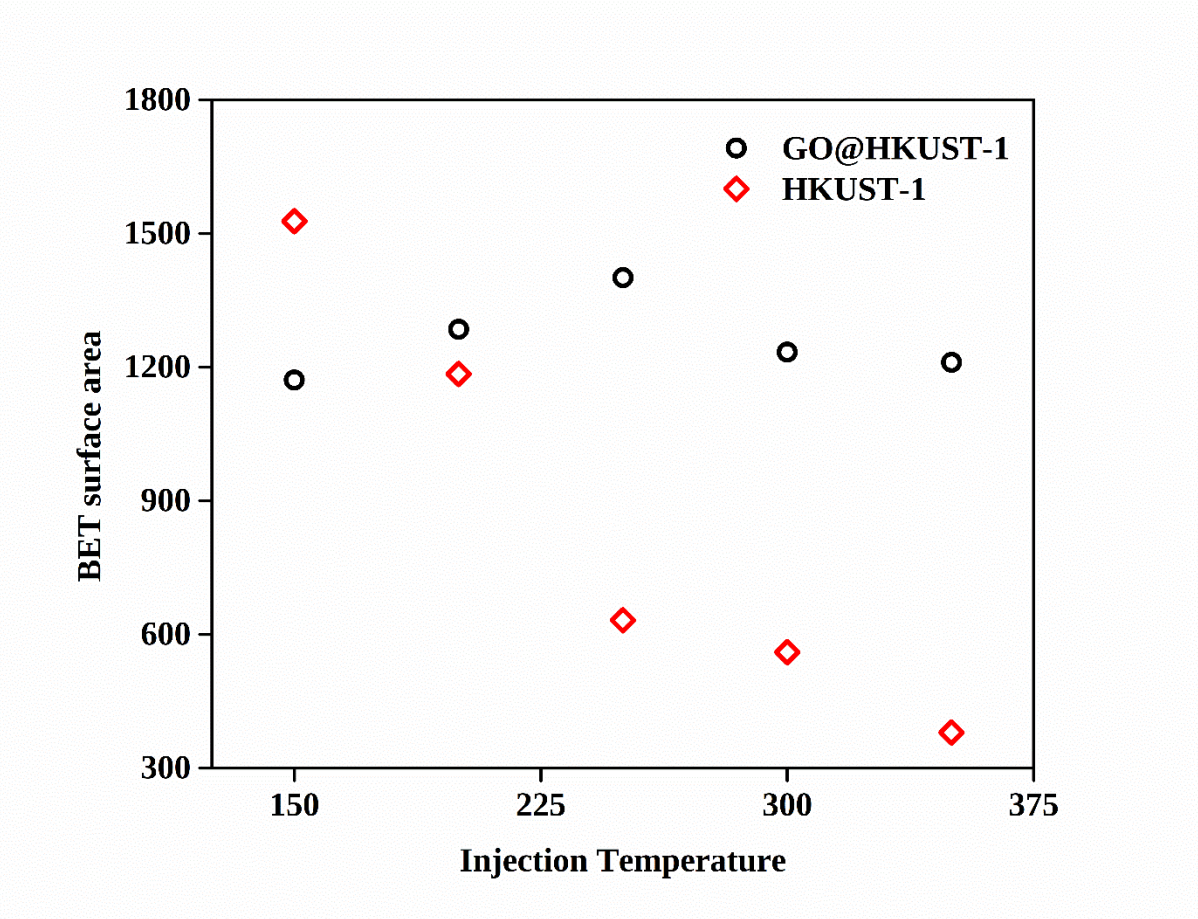

Figure 3-8: HKUST-1 and GO@HKUST-1 Properties: BET surface area vs. scCO₂ injection temperature.

The samples underwent consistent activation before their specific surface area and porosity were determined using the Micromeritics ASAP 2020 instrument. The pore sizes were calculated using the Barrett-Joyner-Halenda (BJH) method, and Figure 3-8 showed that the samples had BET surface areas ranging from 1171 - 1401 $m^2.g^{-1}$. The CO_2 injection temperature directly correlated with surface area, with the highest value achieved at T_{inj} = 250 °C. However, increasing the synthesis temperature beyond this point caused a decrease in BET surface area due to the formation of agglomerates and a reduction in crystallite

size, leading to the decline in the available surface area for gas adsorption. It is, therefore, essential to understand the mixing and temperature distribution in the reactor to achieve a high surface area and porosity, which are essential for gas adsorption and separation. The nitrogen adsorption-desorption measurements and BJH analysis provide useful information on the physical properties of the synthesized materials, aiding in the optimization of the synthesis process for specific material properties.

Table 3- 3: GO@HKUST-1 Properties: Comparison of synthesis methods of the GO@HKUST-1 MOF, including surface area (SA) and SAPR.

Synthesis Method	SA ($m^2.g^{-1}$)	SAPR ($m^2.m^{-3}.d^{-1}$)	Reference
Microwave heating	BET 1080	$7.46*10^6$	[122]
Ultrasound irradiation	BET 1,156	$4.79*10^8$	[122]
Mechano-chemical	BET 1421	$2.95*10^7$	[123]
Conventional solvothermal	BET 1000-1800	$5.76*10^6$	[124]
Electro-chemical	BET 1,500-2100	$5.81*10^6$	[125]
Continuous flow - Ultra-fast $scCO_2$	BET 1401	$5.36*10^{10}$	This research

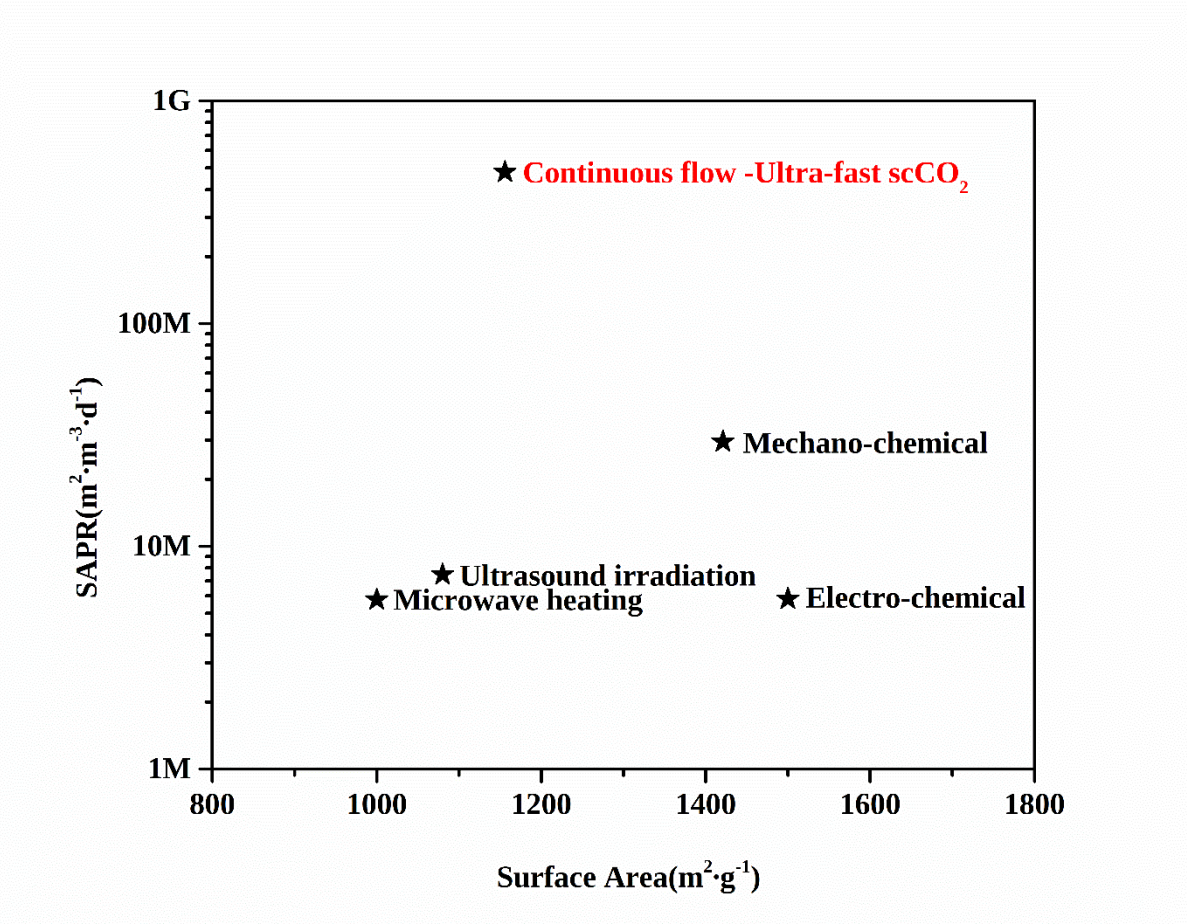

Figure 3-9: GO@HKUST-1 Properties: SAPR vs. SA plot.

The quest for optimal synthesis methods of MOFs is challenging and riddled with several factors that can impact the efficacy of the process. The precursors' compositions and the varying molar ratios employed across methods pose significant hurdles. Moreover, even the characterization of fundamental morphology parameters such as particle size, uniformity, and surface area can be influenced by the measurement techniques employed, further compounding the challenge. Numerous metrics have been used to pursue the most effective synthesis methods, including reaction time, space-time yield (STY), and surface area production rate (SAPR). In Table 3- 3 and Figure 3-9, the results of these metrics are presented for different synthesis methods. The results of this study indicate that the $scCO_2$ synthesis method with a reaction time of ~650 ms achieved the highest surface area production rate (SAPR) compared to other methods. However, this came with a trade-off, as the BET surface area of the material

was reduced to 1401 $m^2 g^{-1}$. The race to balance synthesis parameters for optimal MOF properties continues, but these findings serve as a testament to the persistence and ingenuity of the scientific community.

3.4 Conclusion

This study synthesized GO@HKUST-1 hybrid nanocomposites. Qualitative assessments confirmed that the formation of GO@HKUST-1 did not alter the structure of the parent MOF. The resultant nanocomposites exhibited similar characteristics to those of pure HKUST-1. The main findings are that GO@HKUST-1 nanocomposites exhibited superior thermal properties of HKUST-1 and a broader synthesis envelope. Potential control of the particle size needs to be further evaluated.

Chapter 4 Continuous Flow Synthesis of MWCNT@HKUST-1 Hybrid Composites in scCO$_2$ Environment: Effects of Injection Temperature on Morphology, Crystallinity, and Porosity.

4.1 Introduction

When exposed to moisture, HKUST-1 exhibits a significant decrease in its surface area and absorption capacity. An effective technique for improving the adsorption characteristics and stability of HKUST-1 involves modifying the material through functionalization. [134] Incorporating diverse functional groups have been shown to produce superior CO_2 capture properties.[135] Another approach to functionalization is the creation of hybrid functionalized materials, or composites, by combining HKUST-1 materials with other crystalline structures like multi-walled carbon nanotubes (MWCNTs). [13, 81-83, 116, 117, 126, 134] Synthesizing composites that combine carbon nanotubes (CNTs) and MOFs have displayed encouraging outcomes in gas storage applications. In an ideal scenario, such composites would also exhibit greater thermal resistance than pure HKUST - 1. [1, 2, 4, 8, 117]

MOF - based composites have mostly been about growing MOFs on siliceous materials[136] or adding carbon to MOFs. [137, 138] For instance, Yang et al. prepared a CNT/MOF-5 hybrid composite and observed a significant increase in surface area and hydrogen storage capacity compared to MOF-5. [138] Xiang et al. synthesized CNT/HKUST-1 hybrid that showed increased CO_2 and CH_4 uptakes compared to unmodified MOFs. [1]

Recently, the incorporation of MWCNTs into MOFs has been reported to be promising for the adsorption and separation of gases. Zhonghua et al. reported the incorporation of MWCNTs into HKUST-1 for CO_2 capture. [134] Unmodified and CNT@$Cu_3(BTC)_2$ showed CO_2 adsorption capacities of 295 and 595 mg g^{-1} at 25°C and 18 bar, respectively. Prasanth et al. offer a prime example of the composite MOF synthesis approach, where single-walled carbon nanotubes (SWCNTs) were incorporated into MIL - 101 to produce a new MOF material

(SWNT@MIL-101). [139] Remarkably, the structure of the MOF material was unaltered by the incorporation of SWCNTs, and the hydrogen (H_2) adsorption capacity of MIL - 101 increased from 6.37 to 9.18 wt% at 77 K and 60 bar, and from 0.23 to 0.64 wt% at T = 298 K and P – 60 bar.

Developing composites based on HKUST-1 has become an active and attractive field of research. Several new and exciting examples have emerged, including H_2 storage, catalysis, chromatography, CO_2 capture, and lithium-sulfur batteries. Nevertheless, synthesizing these composite materials takes several hours using the conventional method. We aim to expedite the synthesis process of these composites. This chapter presents the first use of $scCO_2$ in a continuous flow reactor to synthesize, for the first time to our knowledge, a composite material named MWCNT@HKUST-1 based on MWCNTs and HKUST-1, utilizing the $scCO_2$ synthesis environment. In five experiments, we investigate the effects of $scCO_2$ mixing section injection temperature (ranging from T_{inj} = 150 to 350°C) on the morphology, crystallinity, and porosity of the MWCNT@HKUST-1.

4.2 Experimental Procedure

The reactor's design has been documented in section 2.2.1, with a brief explanation provided here. The flow diagram of the reactor can be found in Figure 2 - 1. This continuous-flow reactor is precisely engineered to operate within a temperature range of T = 298-873K (25 – 600 °C) and a pressure range of P = 0.10 – 30 MPa. In the synthesis process, two unheated precursor streams, namely metal and organic precursors, are combined with heated $scCO_2$ in the counterflow mixing section to rapidly mix and heat the reactants. Subsequently, the effluent is rapidly cooled to ambient temperature and passed through a BPR. The reaction products remain in the liquid phase, while the CO_2 is naturally aspirated into the fume hood.

The Benzene-1,3,5-tricarboxylic acid (BTC) and Copper (II) nitrate trihydrate, Cu $(NO_3)_2$•$3H_2O$ utilized in this experiment were obtained from Sigma-Aldrich. The Aligned MWCNTs (95%+ purity, outer diameter 10 – 20 nm, length 30 - 1000 micrometer) used in this study were procured from Nanostructured & Amorphous Materials Inc. The concentration of the precursor remained constant throughout the process. The MOF particles were isolated through centrifugation using an Allegra X-30 centrifuge from Bechman Coulter, operating at 9,000 rotations per minute for 10 minutes. The MOFs were placed in glass vials and subjected to overnight drying at 393 K.

Five experiments were performed to investigate the influence of scCO2 injection temperature on the physisorption of CNT@HKUST-1. The injection temperatures (T_{inj}) were varied between 150°C to 350°C to determine the temperature range suitable for MOFs formation while avoiding the collapse of CNT@HKUST-1 MOFs into Cu_2O. A constant pressure of P = 10 MPa was maintained in the reactor during experiments, while the flow rates of the precursor pumps (Pump 1 and Pump 2) and $scCO_2$ flow rate (Pump 3) remained consistent at 10 mL min^{-1}, 10 mL min^{-1}, and 25 mL min^{-1}, respectively.

4.3 Results and discussion

The PXRD spectra of HKUST-1 and CNT@HKUST-1 were analyzed and presented in Figure 4 - 1. The PXRD peaks observed in the HKUST-1 patterns were consistent with those reported in the literature, indicating a well-crystallized structure consisting of $Cu_2(OAc)_4$ paddlewheel secondary building units (SBUs) connected by tri-dentate BTC ligands.[9, 67, 73, 112] Here, $Cu_2(OAc)_4$ represents a copper-based coordination compound, where OAc stands for acetate anion. The space group was determined to be Fm3m, with lattice parameters of a = 26.343 Å and V = 1.828×10^{-4} Å. These same peaks were also present in the PXRD patterns of the composite materials, suggesting that the cubic crystalline structure of HKUST-1 was preserved after the incorporation of CNTs. The characteristic (002) peak of CNTs, typically observed at

2θ = 26-27°, was not detected in the diffraction patterns of the composite, likely due to overlapping with the HKUST-1 peak. [138]

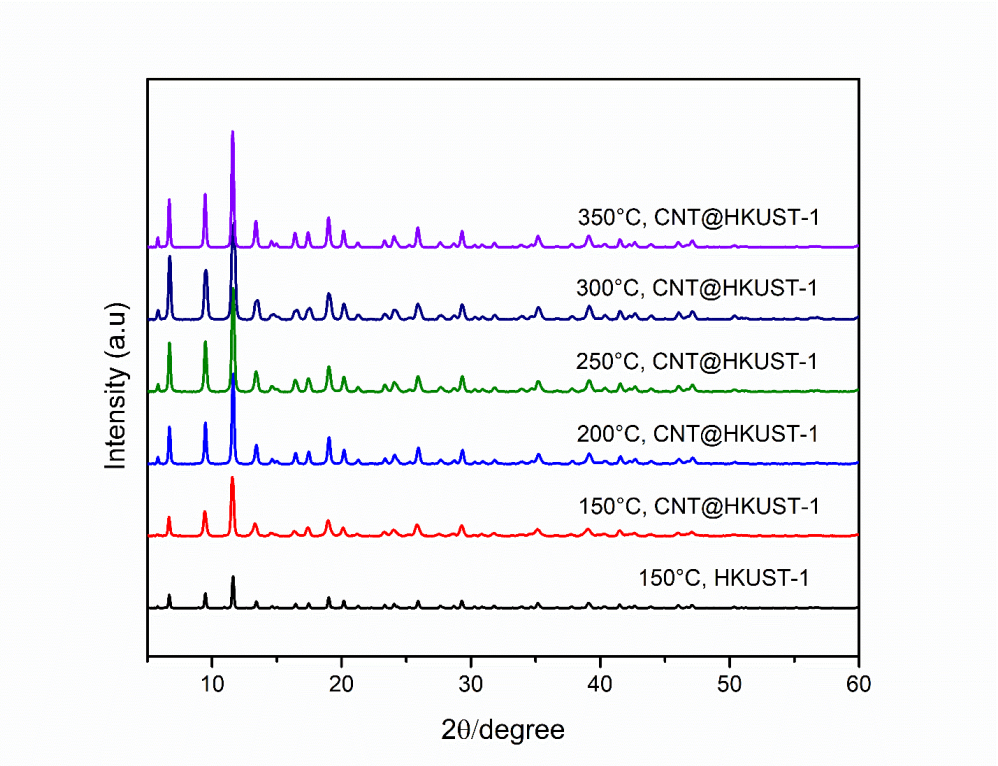

Figure 4 - 1: PXRD spectra of HKUST-1 and 5 wt % MWCNT@HKUST-1 Samples. The pattern shows characteristic peaks corresponding to the crystal lattice planes of the CNTs and HKUST-1. The CNTs in the composite have a characteristic peak at around 2θ = 26°, corresponding to the (002) plane of the hexagonal graphite structure. This peak is broadened due to the small size and high degree of disorder of the CNTs in the composite. The HKUST-1 MOF material in the composite exhibits several sharp peaks in the XRD pattern, indicating its well-defined crystal structure. The most substantial peak in the pattern appears at around 2θ = 12.9°, corresponding to the (111) plane of the MOF structure.

HKUST-1 structure consists of three different cavities that can interconnect to form channels. The largest channel displays Cu−OH_2···H_2O−Cu distances of 19.88 Å between vertices of the cuboctahedral cavity, the second channel exhibits Cu···Cu distances of 18.62 Å, and the smallest channel has COO···COO distances of 15.89 Å. These dimensions suggest that the channels in HKUST-1 are not large enough to host MWCNTs. Instead, it is more likely that MWCNTs serve as a growing template or crystallization seed for HKUST-1, a phenomenon observed in various MOF-coated nanostructures for different applications. [9, 67, 73, 112]

Figure 4 - 2 shows an SEM image, whereas Figure 4 - 3 presents energy-dispersive X-ray spectroscopy (EDS) mapping of the 5% MWCNT@HKUST-1 composite material. The SEM

image shows highly organized particles with an average size of 2 – 6 µm. Note that the particle size is significantly smaller than unmodified HKUST-1 and GO@HKUST-1. The EDS mapping of the copper and carbon elements indicates the presence of Cu^{2+} ions distributed within the analyzed particles.

The morphology of the MCNT@HKUST-1 composite observed in Figure 4 - 2 exhibits a confinement growth of HKUST-1 in MWCNT arrays. Confinement growth refers to the process by which a material is grown or synthesized in a confined space or under restricted growth conditions. It is noteworthy that the crystal size of HKUST-1 in the confined growth is much smaller (sub-micron) than that of the unmodified HKUST - 1. The alteration in HKUST - 1 morphology by growing in the confined interspace of MWCNT is significant in some applications, such as Hydrogen storage.

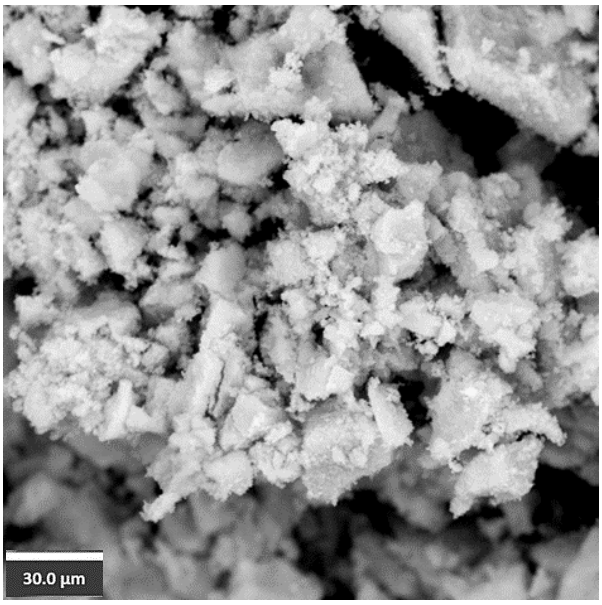

a

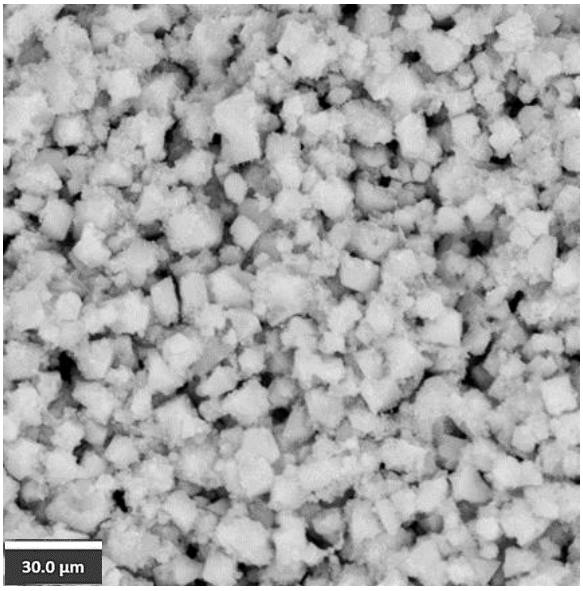

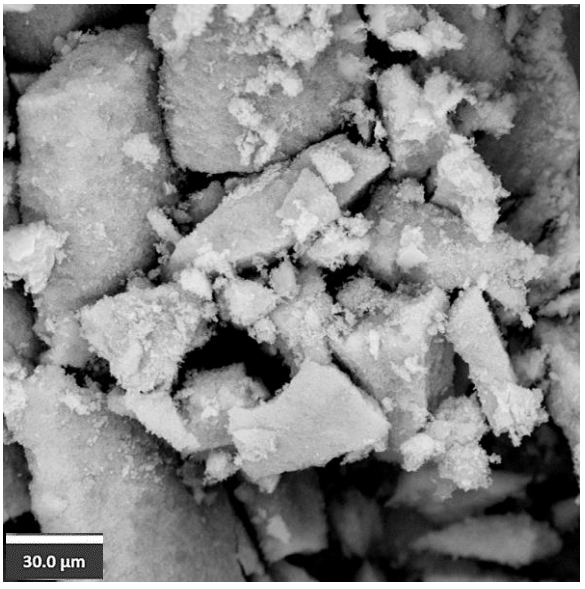

b c

Figure 4 - 2: SEM micrograph of CNT@HKUST-1 synthesized by a continuous flow $scCO_2$ reactor at varying synthesis temperatures: a) T_{inj} = 150 ºC, b) T_{inj} = 250 ºC, c) T_{inj} = 350 ºC.

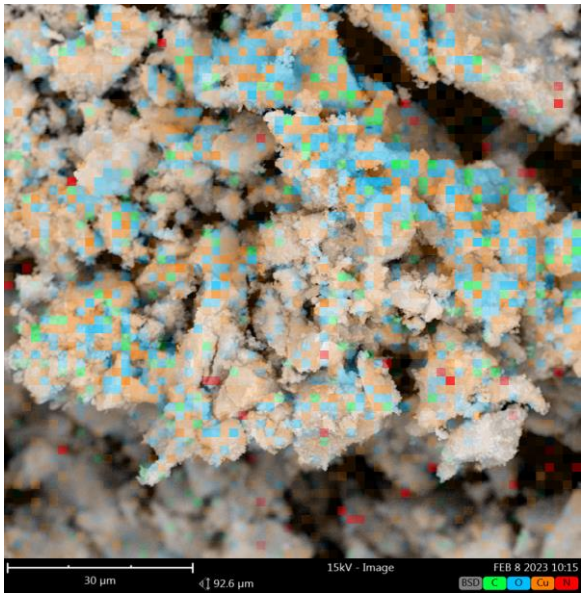

Figure 4 - 3: EDS mapping of CNT@HKUST-1 synthesized at 150 ºC

The elemental analysis results for HKUST-1 and CNT@HKUST-1 are presented in Table 4- 1 and Table 4- 2. The increase in carbon content in the composite samples compared to their parent samples confirms the presence of CNT. The atomic percentages for CNT@HKUST-1 reveal that carbon is the most abundant element, with a concentration of 47.89%, followed by oxygen (34.73%) and nitrogen (4.64%). Despite copper's low atomic concentration (8.68%), its weight percentage in the compound is substantial (30.63%), indicating that copper atoms in HKUST-1 play a significant role in determining the material's mass. The elemental analysis results provide valuable insights into the composition of CNT@HKUST-1 and underscore the importance of considering both atomic and weight concentrations when characterizing composite materials.

Table 4- 1: Weight concentration-based elemental analysis

Sample	% Carbon	%Copper	%Hydrogen	%Nitrogen	%Oxygen
150°C, HKUST-1	51.10	16.42	6.07	11.10	34.57
250°C, CNT@HKUST-1	47.89	8.68	2.06	4.64	34.73

Table 4- 2: Atomic concentration-based elemental analysis

Sample	% Carbon	%Copper	%Hydrogen	%Nitrogen	%Oxygen
150°C, HKUST-1	36.54	29.30	6.06	10.91	30.07
250°C, CNT@HKUST-1	32.98	30.63	3.99	3.61	29.79

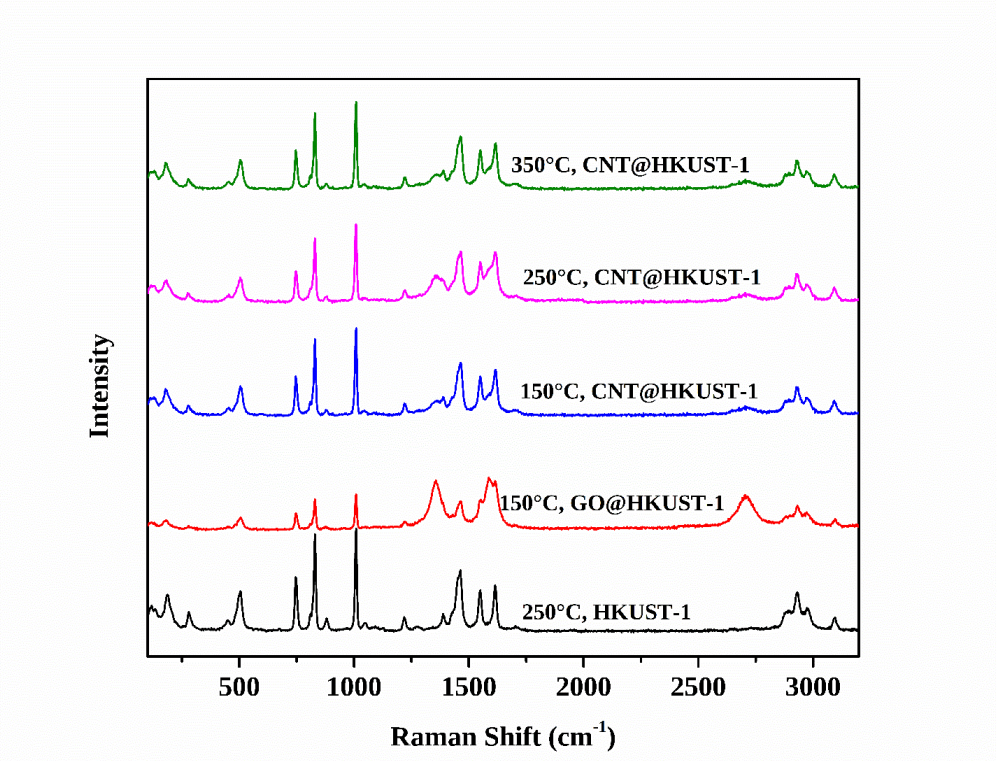

Figure 4 - 4: Raman spectra for HKUST-1 and 5 wt % MWCNT@ HKUST-1.

Raman spectroscopy experiments on the MWCNT@HKUST-1 composite provided insights into incorporating MWCNTs with HKUST-1. The characteristic stretching vibration modes of the CNTs were observed in Figure 4 - 4, confirming the presence of MWCNTs in the composite. The G band appears at around 1580 cm^{-1} and is associated with the stretching vibration of sp^2 carbon atoms in the graphene lattice of the CNTs. The D band appears at around 1350 cm^{-1} and is associated with the disorder-induced breathing mode of the graphene lattice. The intensity ratio of the D band to the G band (ID/IG) can be used to measure the degree of disorder and defects in the CNTs.

In addition to the characteristic peaks of the MWCNTs, typical HKUST-1 Raman peaks were also observed in the spectrum. The peaks associated with the C-C modes of the benzene ring appeared at 1003 and 1610 cm^{-1}, with the latter appearing as a shoulder next to the G-band from the MWCNTs in the MWCNT@HKUST-1 composite spectra. The symmetric and asymmetric −COO modes of the carboxylates appeared at 1460 and 1540 cm^{-1}, respectively. The signals from the MWCNT@HKUST-1 composite red-shifted to 1427 and 1527 cm^{-1}, which suggests that the presence of the MWCNTs may have some effect on the coordination of copper OMS.

The Raman spectrum of the CNT-HKUST-1 composite reveals that the CNTs and HKUST – 1 particle are well-integrated and coexist within the material. The ID/IG ratio of the CNTs in the composite indicates a moderate degree of disorder, which is consistent with the broadening of the CNT peak observed in the XRD pattern. The characteristic peaks in the Raman spectrum confirm the presence of the HKUST-1 MOF particles in the composite.

Overall, the Raman spectroscopy experiments provided valuable information about the vibrational properties of the MWCNT@HKUST-1 composite and the incorporation of MWCNTs in the composite. The information obtained from these experiments can be used to optimize the synthesis and properties of the composite material for various applications.

Fourier-transform infrared (FTIR) spectroscopy is a powerful technique for identifying composite material functional groups. In the case of the CNT@HKUST-1 composite, FTIR experiments were carried out to provide insights into the chemical structure of the composite material. Figure 4 - 5 presents the FTIR spectra of HKUST-1 and CNT@HKUST-1.

The FTIR spectrum of the CNT@HKUST-1 composite showed characteristic peaks of both the CNTs and the HKUST-1 framework. The peaks observed in the spectrum were in good agreement with those reported in previous studies.[138] The peaks associated with the

stretching vibrations of the C-C bond in the CNTs were observed at 1490 cm^{-1}, while the peaks associated with the stretching vibrations of the Cu-O bond in the HKUST-1 framework were observed at 622 cm^{-1}.

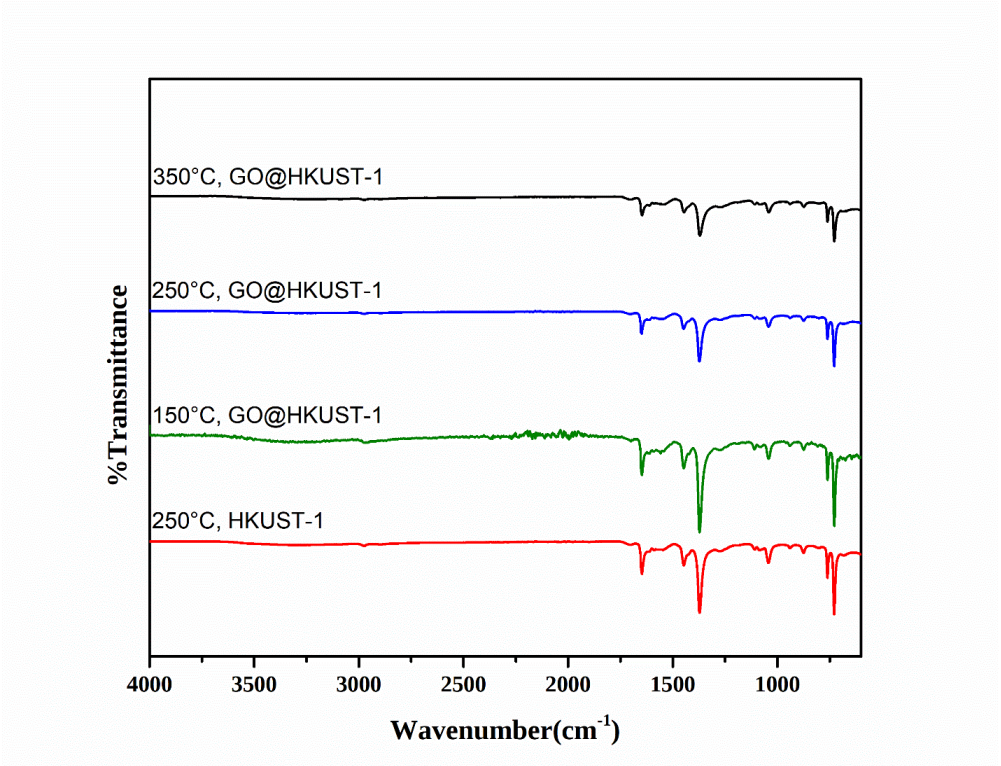

Figure 4 - 5: FTIR spectra for HKUST-1 and 5 wt % MWCNT@ HKUST-1.

The FTIR spectrum also showed additional peaks, which could be attributed to functional groups on the surface of the CNTs and the HKUST-1 framework. The peak observed at 1713 cm^{-1} was assigned to the stretching vibrations of the carbonyl group (C=O) in the carboxylate group of HKUST-1. Additionally, the peak observed at 1640 cm^{-1} can be attributed to the bending vibrations of the N-H bond in the HKUST-1 framework.

The FTIR experiments provided valuable information about the chemical structure of the CNT@HKUST-1 composite and the functional groups present in the composite. The information obtained from these experiments can be used to optimize the synthesis and properties of the composite material for various applications.

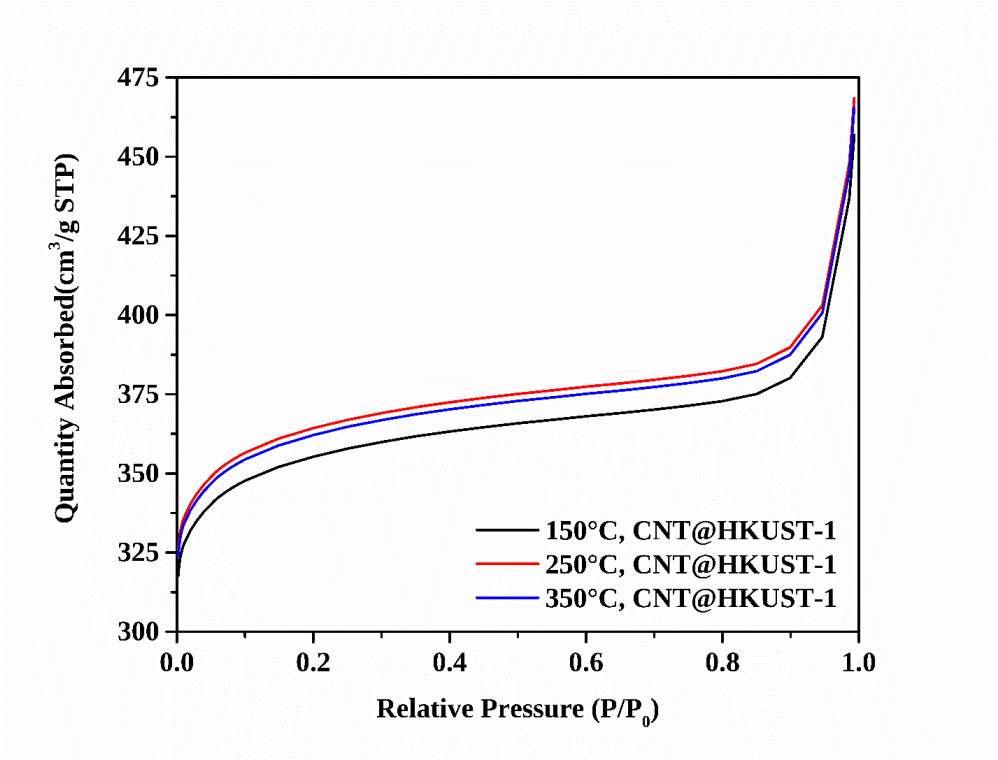

Figure 4 - 6: Nitrogen adsorption isotherms of the synthesized CNT@HKUST-1.Which provides information about its gas storage properties. The particles' uniform pore size and microporosity were identified by analyzing the isotherms' shape.

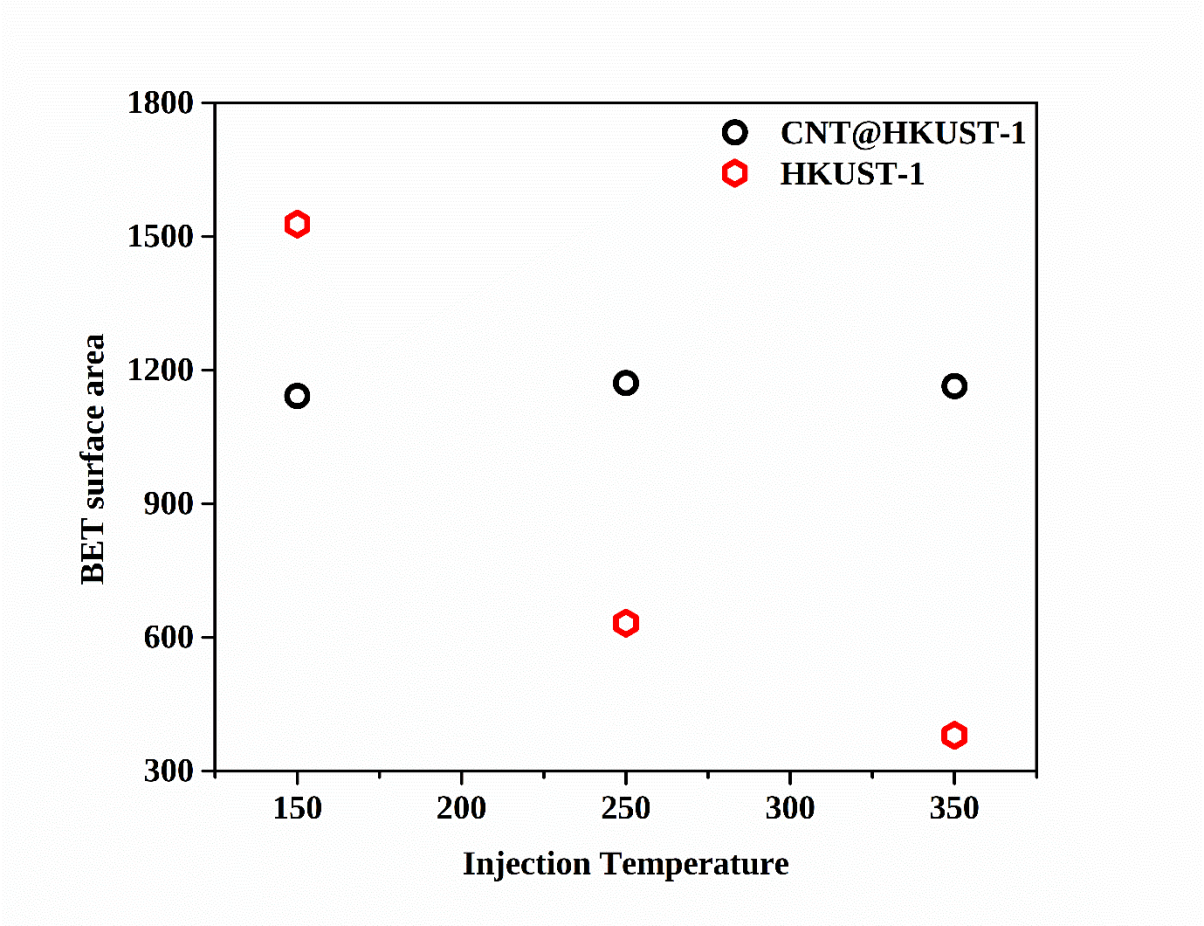

Figure 4 - 7: HKUST-1 and CNT@HKUST-1 Properties: BET surface area vs. $scCO_2$ injection temperature.

For CNT@HKUST-1, N_2 adsorption-desorption experiments were performed at 77 K to evaluate the surface area and porosity of the samples. According to the IUPAC classification, Type-I shape isotherm is identified in Figure 4 - 6. This isotherm shape indicates microporosity and uniform pore sizes. Hysteresis loops of type H4 were observed for all materials, which is associated with the filling of micropores. While the pores of HKUST-1 are almost cylindrical, the incorporation of CNTs caused a slight change in the shape of the hysteresis loop. This alteration in shape resulted from an enlargement of the pore size, which caused an increase in capillary condensation. Further analysis revealed that the composite with 5 wt % MWCNT has approximately 25% lower surface area and pore volume than HKUST-1 when the injection temperature is 423 K, and with the increasing injection temperature, the BET surface area of 5 wt % MWCNT@HKUST-1 shows very little change. Overall, these findings demonstrate

the potential for CNTs to enhance the surface area and pore volume of HKUST-1, which could have important implications for applications in various fields such as gas storage, catalysis, and drug delivery.

4.4 Conclusion

This research aimed to synthesize CNT/HKUST-1 hybrid nanocomposites for gas storage applications. The study showed that the formation of CNT@HKUST-1 did not alter the structure of the MOF, and the resulting nanocomposites exhibited comparable properties to pure HKUST-1, with improved surface area for certain synthesis conditions. Although adjusting the injection temperature of $scCO_2$ had only a minor effect on the BET surface area, further research should be conducted to explore the impact of varying the concentration of reactants. Using $scCO_2$ as a heating and mixing medium in a continuous flow reactor proved highly reliable, resulting in no leftover reactants or undesired by-products in the final product. The study suggests that CNT@HKUST-1 nanocomposites have promising potential for gas storage applications.

Chapter 5 Conclusions

Despite identifying thousands of MOFs, only a few are currently produced commercially. However, the potential applications of MOFs are vast and promising, and their practical uses remain largely unexplored. Therefore, further research and development efforts are crucial to unlocking the full potential of MOFs for practical applications.

Several crucial steps must be taken to exploit the practical applications of MOFs. Firstly, developing efficient and scalable synthesis methods is essential to enable the large-scale production of MOFs. This will allow MOFs to be produced in large quantities at affordable prices, making them more accessible for commercial applications.

Secondly, comprehensive characterization techniques are necessary to understand MOFs' structural and functional properties. These techniques will enable researchers to fully characterize and understand the physicochemical properties of MOFs, which is critical for designing MOFs with tailored properties for specific applications.

Finally, it is crucial to test MOFs under practical conditions to ensure they perform as expected in real-world applications. This will help establish MOFs' practical uses and efficacy in various fields. Furthermore, the successful application of MOFs in different industries will pave the way for the widespread commercial use of MOFs.

In conclusion, further research and development are needed to explore the potential of MOFs for practical applications. Developing efficient and scalable synthesis methods, comprehensive characterization techniques, and testing under realistic conditions is crucial to realizing the practical uses of MOFs. With continued efforts, MOFs can become a vital material for various industries, ranging from energy storage to drug delivery, thereby contributing to the betterment of society.

Chapter 6 Future work

1. Scale-up of the process:

The continuous flow $scCO_2$ reactor has shown promising results for the sub-second formation of MOF composites at the laboratory scale. However, the commercial production of the composite requires the scalability of the process. The scalability of the process can be achieved by increasing the size of the reactor, improving the efficiency of the extraction and purification steps, and optimizing the operating conditions. The reactor size can be expanded using a larger high-pressure vessel that can accommodate a higher volume of $scCO_2$. The extraction and purification steps can be improved using more efficient techniques such as ultrafiltration. The operating conditions such as temperature, pressure, flow rate, and residence time can be optimized to obtain high yields and purity of the composite. Successful scale-up of the process can lead to the commercial production of MOF composite for various applications.

2. Optimization of process parameters:

The synthesis of MOF composite using a continuous flow $scCO_2$ reactor involves several process parameters such as temperature, pressure, flow rate, and residence time. Optimizing these process parameters can result in improved properties of the composite, such as higher yield, higher purity, and enhanced performance. Statistical techniques such as the Design of Experiments (DoE) can be used to study the effect of each process parameter on the synthesis process. DoE can help identify the optimal process conditions by minimizing the required experiments. The optimized process conditions can result in an efficient and reproducible synthesis of MOF composite, which can be helpful in various applications.

3. Application of the composite:

The MOF composite can be evaluated for its potential applications in various fields, such as catalysis, gas separation, energy storage, and drug delivery. The composite's performance can be compared with existing materials to determine its advantages and limitations. The composite's catalytic activity can be evaluated by studying its ability to catalyze various chemical reactions. The composite's gas separation properties can be assessed by measuring its selectivity and permeability for different gases. The composite's energy storage potential can be evaluated by studying its capacitance and cycle stability in supercapacitors. The composite's drug delivery potential can be evaluated by studying its ability to encapsulate and release drugs.

4. Synthesis of three-dimensional (3D) MOF composite:

The current synthesis process of MOF composite produces a two-dimensional (2D) composite. However, synthesizing a three-dimensional (3D) composite can enhance the specific surface area and improve the performance of the composite in various applications such as gas adsorption and separation. The synthesis of a 3D composite is challenging as it requires the development of a suitable template to guide the growth of the composite in three dimensions. Developing a suitable template can involve various techniques, such as using sacrificial templates, self-assembling block copolymers, and electrospinning. The 3D composite's performance can be evaluated by comparing its specific surface area, gas adsorption capacity, and selectivity with the 2D composite. The successful synthesis of a 3D MOF composite can open new avenues for its applications in various fields.

Chapter 7 Bibliography

[1] X. Lin, N. R. Champness, and M. Schröder, "Hydrogen, methane and carbon dioxide adsorption in metal-organic framework materials," *Functional Metal-Organic Frameworks: Gas Storage, Separation and Catalysis,* pp. 35-76, 2010.

[2] S. Ma and H.-C. Zhou, "Gas storage in porous metal–organic frameworks for clean energy applications," *Chemical Communications,* vol. 46, no. 1, pp. 44-53, 2010.

[3] J.-R. Li, R. J. Kuppler, and H.-C. Zhou, "Selective gas adsorption and separation in metal–organic frameworks," *Chemical Society Reviews,* vol. 38, no. 5, pp. 1477-1504, 2009.

[4] L. Ma and W. Lin, "Designing metal-organic frameworks for catalytic applications," *Functional metal-organic frameworks: gas storage, separation and catalysis,* pp. 175-205, 2010.

[5] J. Lee, O. K. Farha, J. Roberts, K. A. Scheidt, S. T. Nguyen, and J. T. Hupp, "Metal–organic framework materials as catalysts," *Chemical Society Reviews,* vol. 38, no. 5, pp. 1450-1459, 2009.

[6] R. C. Huxford, J. Della Rocca, and W. Lin, "Metal–organic frameworks as potential drug carriers," *Current opinion in chemical biology,* vol. 14, no. 2, pp. 262-268, 2010.

[7] J. A. Hurd, R. Vaidhyanathan, V. Thangadurai, C. I. Ratcliffe, I. L. Moudrakovski, and G. K. H. Shimizu, "Anhydrous proton conduction at 150 C in a crystalline metal–organic framework," *Nature chemistry,* vol. 1, no. 9, pp. 705-710, 2009.

[8] N. Roques, V. Mugnaini, and J. Veciana, "Magnetic and porous molecule-based materials," *Functional Metal-Organic Frameworks: Gas Storage, Separation and Catalysis,* pp. 207-258, 2010.

[9] K.-S. Lin, A. K. Adhikari, C.-N. Ku, C.-L. Chiang, and H. Kuo, "Synthesis and characterization of porous HKUST-1 metal organic frameworks for hydrogen storage," *International journal of hydrogen energy,* vol. 37, no. 18, pp. 13865-13871, 2012.

[10] M. P. Suh, H. J. Park, T. K. Prasad, and D.-W. Lim, "Hydrogen storage in metal–organic frameworks," *Chemical reviews,* vol. 112, no. 2, pp. 782-835, 2012.

[11] A. U. Czaja, N. Trukhan, and U. Müller, "Industrial applications of metal–organic frameworks," *ChSRv,* vol. 38, no. 5, pp. 1284-1293, 2009.

[12] U. Mueller, M. Schubert, F. Teich, H. Puetter, K. Schierle-Arndt, and J. Pastre, "Metal–organic frameworks—prospective industrial applications," *Journal of Materials Chemistry,* vol. 16, no. 7, pp. 626-636, 2006.

[13] N. Keshmiri, P. Najmi, M. Ramezanzadeh, and B. Ramezanzadeh, "Designing an eco-friendly lanthanide-based metal organic framework (MOF) assembled graphene-oxide with superior active anti-corrosion performance in epoxy composite," *Journal of Cleaner Production,* vol. 319, p. 128732, 2021.

[14] W. Morris *et al.*, "Role of modulators in controlling the colloidal stability and polydispersity of the UiO-66 metal–organic framework," *ACS applied materials & interfaces,* vol. 9, no. 39, pp. 33413-33418, 2017.

[15] J. H. Cavka *et al.*, "A new zirconium inorganic building brick forming metal organic frameworks with exceptional stability," *Journal of the American Chemical Society,* vol. 130, no. 42, pp. 13850-13851, 2008.

[16] Y. Yan *et al.*, "A mesoporous metal–organic framework constructed from a nanosized C 3-symmetric linker and [Cu 24 (isophthalate) 24] cuboctahedra," *Chemical Communications,* vol. 47, no. 36, pp. 9995-9997, 2011.

[17] M. Kim, J. A. Boissonnault, C. A. Allen, P. V. Dau, and S. M. Cohen, "Functional tolerance in an isoreticular series of highly porous metal–organic frameworks," *Dalton Transactions,* vol. 41, no. 20, pp. 6277-6282, 2012.

[18] S. H. Jhung, J. H. Lee, P. M. Forster, G. Férey, A. K. Cheetham, and J. S. Chang, "Microwave Synthesis of Hybrid Inorganic–Organic Porous Materials: Phase-Selective and Rapid Crystallization," *Chemistry–A European Journal,* vol. 12, no. 30, pp. 7899-7905, 2006.

[19] J. Rocha, L. D. Carlos, F. A. A. Paz, and D. Ananias, "Luminescent multifunctional lanthanides-based metal–organic frameworks," *Chemical Society Reviews,* vol. 40, no. 2, pp. 926-940, 2011.
[20] S. L. James *et al.*, "Mechanochemistry: opportunities for new and cleaner synthesis," *Chemical Society Reviews,* vol. 41, no. 1, pp. 413-447, 2012.
[21] T. N. Glasnov and C. O. Kappe, "Microwave-assisted synthesis under continuous-flow conditions," *Macromolecular rapid communications,* vol. 28, no. 4, pp. 395-410, 2007.
[22] S. Kumar, S. Jain, M. Nehra, N. Dilbaghi, G. Marrazza, and K.-H. Kim, "Green synthesis of metal–organic frameworks: A state-of-the-art review of potential environmental and medical applications," *Coordination Chemistry Reviews,* vol. 420, p. 213407, 2020.
[23] M. Khatami and S. Iravani, "Green and eco-friendly synthesis of nanophotocatalysts: an overview," *Comments on Inorganic Chemistry,* vol. 41, no. 3, pp. 133-187, 2021.
[24] P. Rani and R. Srivastava, "Comprehensive Understanding of the Eco-Friendly Synthesis of Zeolites: Needs of 21st Century Sustainable Chemical Industries," *The Chemical Record,* vol. 20, no. 9, pp. 968-988, 2020.
[25] J. Hartwig, J. B. Metternich, N. Nikbin, A. Kirschning, and S. V. Ley, "Continuous flow chemistry: a discovery tool for new chemical reactivity patterns," *Organic & Biomolecular Chemistry,* vol. 12, no. 22, pp. 3611-3615, 2014.
[26] D. E. Fitzpatrick, C. Battilocchio, and S. V. Ley, "Enabling technologies for the future of chemical synthesis," *ACS central science,* vol. 2, no. 3, pp. 131-138, 2016.
[27] A. Hafner, V. Mancino, M. Meisenbach, B. Schenkel, and J. Sedelmeier, "Dichloromethyllithium: synthesis and application in continuous flow mode," *Organic letters,* vol. 19, no. 4, pp. 786-789, 2017.
[28] G. Jas and A. Kirschning, "Continuous flow techniques in organic synthesis," *Chemistry–A European Journal,* vol. 9, no. 23, pp. 5708-5723, 2003.
[29] R. M. Myers, D. E. Fitzpatrick, R. M. Turner, and S. V. Ley, "Flow chemistry meets advanced functional materials," *Chemistry–A European Journal,* vol. 20, no. 39, pp. 12348-12366, 2014.
[30] M. Rubio-Martinez *et al.*, "Versatile, high quality and scalable continuous flow production of metal-organic frameworks," *Scientific Reports,* vol. 4, no. 1, p. 5443, 2014.
[31] M. Rubio-Martinez, C. Avci-Camur, A. W. Thornton, I. Imaz, D. Maspoch, and M. R. Hill, "New synthetic routes towards MOF production at scale," *Chemical Society Reviews,* vol. 46, no. 11, pp. 3453-3480, 2017.
[32] A. S. Munn, P. W. Dunne, S. V. Y. Tang, and E. H. Lester, "Large-scale continuous hydrothermal production and activation of ZIF-8," *Chemical communications,* vol. 51, no. 64, pp. 12811-12814, 2015.
[33] T. Adschiri and A. Yoko, "Supercritical fluids for nanotechnology," *The Journal of Supercritical Fluids,* vol. 134, pp. 167-175, 2018.
[34] K. Sue *et al.*, "Size-controlled synthesis of metal oxide nanoparticles with a flow-through supercritical water method," *Green Chemistry,* vol. 8, no. 7, pp. 634-638, 2006.
[35] T. Adschiri, Y.-W. Lee, M. Goto, and S. Takami, "Green materials synthesis with supercritical water," *Green Chemistry,* vol. 13, no. 6, pp. 1380-1390, 2011.
[36] E. W. Lemmon, "Thermophysical properties of fluid systems," *NIST chemistry WebBook,* 2010.
[37] A. Cabanas and M. Poliakoff, "The continuous hydrothermal synthesis of nano-particulate ferrites in near critical and supercritical water," *Journal of Materials Chemistry,* vol. 11, no. 5, pp. 1408-1416, 2001.
[38] B. R. Pinkard, D. J. Gorman, K. Tiwari, J. C. Kramlich, P. G. Reinhall, and I. V. Novosselov, "Review of Gasification of Organic Compounds in Continuous-Flow, Supercritical Water Reactors," *Industrial & Engineering Chemistry Research,* vol. 57, no. 10, pp. 3471-3481, 2018.
[39] B. R. Pinkard *et al.*, "Supercritical water gasification: practical design strategies and operational challenges for lab-scale, continuous flow reactors," *Heliyon,* vol. 5, no. 2, p. e01269, 2019.

[40] B. R. Pinkard, J. C. Kramlich, and I. V. Novosselov, "Gasification Pathways and Reaction Mechanisms of Primary Alcohols in Supercritical Water," *ACS Sustainable Chemistry & Engineering,* vol. 8, no. 11, pp. 4598-4605, 2020/03/23 2020, doi: 10.1021/acssuschemeng.0c00445.

[41] B. R. Pinkard, A. L. Purohit, S. J. Moore, J. C. Kramlich, P. G. Reinhall, and I. V. Novosselov, "Partial Oxidation of Ethanol in Supercritical Water," *Industrial & Engineering Chemistry Research,* vol. 59, no. 21, pp. 9900-9911, 2020/05/27 2020, doi: 10.1021/acs.iecr.0c00945.

[42] J. Li, B. R. Pinkard, S. Wang, and I. V. Novosselov, "Review: Hydrothermal treatment of per- and polyfluoroalkyl substances (PFAS)," *Chemosphere,* vol. 307, p. 135888, 2022/11/01/ 2022, doi: https://doi.org/10.1016/j.chemosphere.2022.135888.

[43] B. R. Pinkard, S. Shetty, D. Stritzinger, C. Bellona, and I. V. Novosselov, "Destruction of perfluorooctanesulfonate (PFOS) in a batch supercritical water oxidation reactor," *Chemosphere,* vol. 279, p. 130834, 2021/09/01/ 2021, doi: https://doi.org/10.1016/j.chemosphere.2021.130834.

[44] J. Li, C. Austin, S. Moore, B. R. Pinkard, and I. V. Novosselov, "PFOS destruction in a continuous supercritical water oxidation reactor," *Chem. Eng. J.,* vol. 451, p. 139063, 2023/01/01/ 2023, doi: https://doi.org/10.1016/j.cej.2022.139063.

[45] C. Austin, J. Li, S. Moore, A. Purohit, B. R. Pinkard, and I. V. Novosselov, "Destruction and defluorination of PFAS matrix in continuous-flow supercritical water oxidation reactor: Effect of operating temperature," *Chemosphere,* p. 138358, 2023/03/09/ 2023, doi: https://doi.org/10.1016/j.chemosphere.2023.138358.

[46] M. J. Krause *et al.*, "Supercritical Water Oxidation as an Innovative Technology for PFAS Destruction," *Journal of Environmental Engineering,* vol. 148, no. 2, p. 05021006, 2022.

[47] J. T. McDonough *et al.*, "Validation of supercritical water oxidation to destroy perfluoroalkyl acids," *Remediation Journal,* vol. 32, no. 1-2, pp. 75-90, 2022.

[48] Y. Suehiro, M. Nakajima, K. Yamada, and M. Uematsu, "Critical parameters of {xCO2+ (1− x) CHF3} forx=(1.0000, 0.7496, 0.5013, and 0.2522)," *The Journal of Chemical Thermodynamics,* vol. 28, no. 10, pp. 1153-1164, 1996.

[49] E. G. Rasmussen, J. Kramlich, and I. V. Novosselov, "Scalable Continuous Flow Metal–Organic Framework (MOF) Synthesis Using Supercritical CO2," *ACS Sustainable Chemistry & Engineering,* vol. 8, no. 26, pp. 9680-9689, 2020/07/06 2020, doi: 10.1021/acssuschemeng.0c01429.

[50] U. Shanker, V. Jassal, M. Rani, and B. S. Kaith, "Towards green synthesis of nanoparticles: from bio-assisted sources to benign solvents. A review," *International Journal of Environmental Analytical Chemistry,* vol. 96, no. 9, pp. 801-835, 2016.

[51] N. Portolés-Gil, S. Gowing, O. Vallcorba, C. Domingo, A. M. López-Periago, and J. A. Ayllón, "Supercritical CO2 utilization for the crystallization of 2D metal-organic frameworks using tert-butylpyridine additive," *Journal of CO2 Utilization,* vol. 24, pp. 444-453, 2018.

[52] S. M. Liao and T. S. Zhao, "Measurements of heat transfer coefficients from supercritical carbon dioxide flowing in horizontal mini/micro channels," *J. Heat Transfer,* vol. 124, no. 3, pp. 413-420, 2002.

[53] H. Chen, D. Y. Goswami, and E. K. Stefanakos, "A review of thermodynamic cycles and working fluids for the conversion of low-grade heat," *Renewable and sustainable energy reviews,* vol. 14, no. 9, pp. 3059-3067, 2010.

[54] S. M. Moosavi *et al.*, "Understanding the diversity of the metal-organic framework ecosystem," *Nature communications,* vol. 11, no. 1, pp. 1-10, 2020.

[55] J. Kou and L.-B. Sun, "Nitrogen-doped porous carbons derived from carbonization of a nitrogen-containing polymer: efficient adsorbents for selective CO2 capture," *Industrial & Engineering Chemistry Research,* vol. 55, no. 41, pp. 10916-10925, 2016.

[56] F. N. Al-Rowaili, A. Jamal, M. S. Ba Shammakh, and A. Rana, "A review on recent advances for electrochemical reduction of carbon dioxide to methanol using metal–organic framework

(MOF) and non-MOF catalysts: challenges and future prospects," *ACS Sustainable Chemistry & Engineering,* vol. 6, no. 12, pp. 15895-15914, 2018.

[57] J. L. C. Rowsell and O. M. Yaghi, "Metal–organic frameworks: a new class of porous materials," *Microporous and mesoporous materials,* vol. 73, no. 1-2, pp. 3-14, 2004.

[58] Z. Bacsik, R. Atluri, A. E. Garcia-Bennett, and N. Hedin, "Temperature-induced uptake of CO2 and formation of carbamates in mesocaged silica modified with n-propylamines," *Langmuir,* vol. 26, no. 12, pp. 10013-10024, 2010.

[59] S. E. Morgan, M. L. Willis, G. W. Peterson, J. J. Mahle, and G. N. Parsons, "Green MOF-Fabrics: Benign, Scalable Sorption-Vapor Synthesis of Catalytic Composites to Protect against Phosphorus-Based Toxins," *ACS Sustainable Chemistry & Engineering,* vol. 10, no. 8, pp. 2699-2707, 2022.

[60] Y. Chen, X. Mu, E. Lester, and T. Wu, "High efficiency synthesis of HKUST-1 under mild conditions with high BET surface area and CO2 uptake capacity," *Progress in Natural Science: Materials International,* vol. 28, no. 5, pp. 584-589, 2018.

[61] X. Yan, S. Komarneni, Z. Zhang, and Z. Yan, "Extremely enhanced CO2 uptake by HKUST-1 metal–organic framework via a simple chemical treatment," *Microporous Mesoporous Mater.,* vol. 183, pp. 69-73, 2014.

[62] P. Marino, P. R. Donnarumma, H. A. Bicalho, V. Quezada-Novoa, H. M. Titi, and A. J. Howarth, "A Step toward Change: A Green Alternative for the Synthesis of Metal–Organic Frameworks," *ACS Sustainable Chemistry & Engineering,* vol. 9, no. 48, pp. 16356-16362, 2021.

[63] Z. Guo *et al.*, "Air-flow impacting synthesis of metal organic frameworks: a continuous, highly efficient, large-scale mechanochemical synthetic method," *ACS Sustainable Chemistry & Engineering,* vol. 8, no. 10, pp. 4037-4043, 2020.

[64] R. Qin and H. C. Zeng, "Design and synthesis of supported nanoscale metal–organic frameworks: transformation from transition metal silicates," *ACS Sustainable Chemistry & Engineering,* vol. 6, no. 11, pp. 14979-14988, 2018.

[65] N. Stock and S. Biswas, "Synthesis of metal-organic frameworks (MOFs): routes to various MOF topologies, morphologies, and composites," *Chemical reviews,* vol. 112, no. 2, pp. 933-969, 2012.

[66] M. Ding, X. Cai, and H.-L. Jiang, "Improving MOF stability: approaches and applications," *Chemical Science,* vol. 10, no. 44, pp. 10209-10230, 2019.

[67] E. Biemmi, S. Christian, N. Stock, and T. Bein, "High-throughput screening of synthesis parameters in the formation of the metal-organic frameworks MOF-5 and HKUST-1," *Microporous and Mesoporous Materials,* vol. 117, no. 1-2, pp. 111-117, 2009.

[68] M. Gimeno-Fabra *et al.*, "Instant MOFs: continuous synthesis of metal-organic frameworks by rapid solvent mixing," *Chem Comm,* vol. 48, no. 86, pp. 10642-10644, Nov 7 2012, doi: 10.1039/c2cc34493a.

[69] K. Matsuyama, "Supercritical fluid processing for metal–organic frameworks, porous coordination polymers, and covalent organic frameworks," *The Journal of Supercritical Fluids,* vol. 134, pp. 197-203, 2018.

[70] A. P. Nelson, O. K. Farha, K. L. Mulfort, and J. T. Hupp, "Supercritical processing as a route to high internal surface areas and permanent microporosity in metal− organic framework materials," *Journal of the American Chemical Society,* vol. 131, no. 2, pp. 458-460, 2009.

[71] H. Liu *et al.*, "Role of supercritical carbon dioxide (scCO2) in fabrication of inorganic-based materials: a green and unique route," *Science and Technology of Advanced Materials,* vol. 22, no. 1, pp. 695-717, 2021.

[72] I.-A. Baragau *et al.*, "Efficient continuous hydrothermal flow synthesis of carbon quantum dots from a targeted biomass precursor for on–off metal ions nanosensing," *ACS Sustainable Chemistry & Engineering,* vol. 9, no. 6, pp. 2559-2569, 2021.

[73] E. G. Rasmussen, J. Kramlich, and I. V. Novosselov, "Synthesis of metal-organic framework HKUST-1 via tunable continuous flow supercritical carbon dioxide reactor," *Chem. Eng. J.,* vol. 450, p. 138053, 2022/12/15/ 2022, doi: https://doi.org/10.1016/j.cej.2022.138053.

[74] J. Ren, X. Dyosiba, N. M. Musyoka, H. W. Langmi, M. Mathe, and S. Liao, "Review on the current practices and efforts towards pilot-scale production of metal-organic frameworks (MOFs)," *Coord. Chem. Rev.,* vol. 352, pp. 187-219, 2017.

[75] P. A. Julien, C. Mottillo, and T. Friščić, "Metal–organic frameworks meet scalable and sustainable synthesis," *Green Chem.,* vol. 19, no. 12, pp. 2729-2747, 2017.

[76] U. Ryu *et al.*, "Recent advances in process engineering and upcoming applications of metal–organic frameworks," *Coord. Chem. Rev.,* vol. 426, p. 213544, 2021.

[77] Y. Tao, G. Huang, H. Li, and M. R. Hill, "Magnetic metal–organic framework composites: solvent-free synthesis and regeneration driven by localized magnetic induction heat," *ACS Sustainable Chemistry & Engineering,* vol. 7, no. 16, pp. 13627-13632, 2019.

[78] W. L. Teo, W. Zhou, C. Qian, and Y. Zhao, "Industrializing metal–organic frameworks: Scalable synthetic means and their transformation into functional materials," *Mater. Today,* 2021.

[79] P. W. Dunne, E. Lester, and R. I. Walton, "Towards scalable and controlled synthesis of metal–organic framework materials using continuous flow reactors," *React. Chem. Eng.,* vol. 1, no. 4, pp. 352-360, 2016, doi: 10.1039/c6re00107f.

[80] Q. M. Wang *et al.*, "Metallo-organic molecular sieve for gas separation and purification," *Microporous and mesoporous materials,* vol. 55, no. 2, pp. 217-230, 2002.

[81] J. Pokhrel *et al.*, "CO2 adsorption behavior of amine-functionalized ZIF-8, graphene oxide, and ZIF-8/graphene oxide composites under dry and wet conditions," *Microporous and Mesoporous Materials,* vol. 267, pp. 53-67, 2018.

[82] J. Pokhrel *et al.*, "Cu-and Zr-based metal organic frameworks and their composites with graphene oxide for capture of acid gases at ambient temperature," *Journal of Solid State Chemistry,* vol. 266, pp. 233-243, 2018.

[83] S. Shang *et al.*, "Facile synthesis of CuBTC and its graphene oxide composites as efficient adsorbents for CO2 capture," *Chemical Engineering Journal,* vol. 393, p. 124666, 2020.

[84] C. McKinstry, E. J. Cussen, A. J. Fletcher, S. V. Patwardhan, and J. Sefcik, "Scalable continuous production of high quality HKUST-1 via conventional and microwave heating," *Chemical Engineering Journal,* vol. 326, pp. 570-577, 2017.

[85] S. S. Y. Chui, S. M. F. Lo, J. P. H. Charmant, A. G. Orpen, and I. D. Williams, "A chemically functionalizable nanoporous material [Cu3 (TMA) 2 (H2O) 3] n," *Science,* vol. 283, no. 5405, pp. 1148-1150, 1999.

[86] M. Faustini *et al.*, "Microfluidic approach toward continuous and ultrafast synthesis of metal–organic framework crystals and hetero structures in confined microdroplets," *Journal of the American Chemical Society,* vol. 135, no. 39, pp. 14619-14626, 2013.

[87] O. Shekhah, J. Liu, R. A. Fischer, and C. Wöll, "MOF thin films: existing and future applications," *Chemical Society Reviews,* vol. 40, no. 2, pp. 1081-1106, 2011.

[88] V. Stavila, A. A. Talin, and M. D. Allendorf, "MOF-based electronic and opto-electronic devices," *Chemical Society Reviews,* vol. 43, no. 16, pp. 5994-6010, 2014.

[89] K. Sumida *et al.*, "Carbon dioxide capture in metal–organic frameworks," *Chemical reviews,* vol. 112, no. 2, pp. 724-781, 2012.

[90] J. An and N. L. Rosi, "Tuning MOF CO2 adsorption properties via cation exchange," *Journal of the American Chemical Society,* vol. 132, no. 16, pp. 5578-5579, 2010.

[91] D. Saha, Z. Bao, F. Jia, and S. Deng, "Adsorption of CO2, CH4, N2O, and N2 on MOF-5, MOF-177, and zeolite 5A," *Environmental science & technology,* vol. 44, no. 5, pp. 1820-1826, 2010.

[92] D.-A. Yang, H.-Y. Cho, J. Kim, S.-T. Yang, and W.-S. Ahn, "CO 2 capture and conversion using Mg-MOF-74 prepared by a sonochemical method," *Energy & Environmental Science,* vol. 5, no. 4, pp. 6465-6473, 2012.

[93] M. Yoon, R. Srirambalaji, and K. Kim, "Homochiral metal–organic frameworks for asymmetric heterogeneous catalysis," *Chemical reviews,* vol. 112, no. 2, pp. 1196-1231, 2012.
[94] M. C. Das *et al.*, "A Zn 4 O-containing doubly interpenetrated porous metal–organic framework for photocatalytic decomposition of methyl orange," *Chemical Communications,* vol. 47, no. 42, pp. 11715-11717, 2011.
[95] Z. Hao *et al.*, "One-dimensional channel-structured Eu-MOF for sensing small organic molecules and Cu 2+ ion," *Journal of Materials Chemistry A,* vol. 1, no. 36, pp. 11043-11050, 2013.
[96] Y. Cui *et al.*, "Dual-emitting MOF⊃ dye composite for ratiometric temperature sensing," *Advanced Materials,* vol. 27, no. 8, pp. 1420-1425, 2015.
[97] H. R. Moon, D.-W. Lim, and M. P. Suh, "Fabrication of metal nanoparticles in metal–organic frameworks," *Chemical Society Reviews,* vol. 42, no. 4, pp. 1807-1824, 2013.
[98] G. Lu *et al.*, "Imparting functionality to a metal–organic framework material by controlled nanoparticle encapsulation," *Nature chemistry,* vol. 4, no. 4, pp. 310-316, 2012.
[99] Y. Liu and Z. Tang, "Multifunctional nanoparticle@ MOF core–shell nanostructures," *Advanced Materials,* vol. 25, no. 40, pp. 5819-5825, 2013.
[100] C. Petit and T. J. Bandosz, "Exploring the coordination chemistry of MOF–graphite oxide composites and their applications as adsorbents," *Dalton Transactions,* vol. 41, no. 14, pp. 4027-4035, 2012.
[101] R. Mehek, N. Iqbal, T. Noor, H. Nasir, Y. Mehmood, and S. Ahmed, "Novel Co-MOF/graphene oxide electrocatalyst for methanol oxidation," *Electrochimica Acta,* vol. 255, pp. 195-204, 2017.
[102] F. Ke, L.-G. Qiu, Y.-P. Yuan, X. Jiang, and J.-F. Zhu, "Fe 3 O 4@ MOF core–shell magnetic microspheres with a designable metal–organic framework shell," *Journal of Materials Chemistry,* vol. 22, no. 19, pp. 9497-9500, 2012.
[103] Y. Yang *et al.*, "Litchi-like Fe 3 O 4@ Fe-MOF capped with HAp gatekeepers for pH-triggered drug release and anticancer effect," *Journal of Materials Chemistry B,* vol. 5, no. 43, pp. 8600-8606, 2017.
[104] J. Li *et al.*, "Unprecedented highly efficient capture of glycopeptides by Fe 3 O 4@ Mg-MOF-74 core–shell nanoparticles," *Chemical Communications,* vol. 53, no. 28, pp. 4018-4021, 2017.
[105] Y. Yue *et al.*, "Nanostructured zeolitic imidazolate frameworks derived from nanosized zinc oxide precursors," *Crystal growth & design,* vol. 13, no. 3, pp. 1002-1005, 2013.
[106] W. Li *et al.*, "MOF-derived hierarchical hollow ZnO nanocages with enhanced low-concentration VOCs gas-sensing performance," *Sensors and Actuators B: Chemical,* vol. 225, pp. 158-166, 2016.
[107] M. Zhao *et al.*, "Core–shell palladium nanoparticle@ metal–organic frameworks as multifunctional catalysts for cascade reactions," *Journal of the American Chemical Society,* vol. 136, no. 5, pp. 1738-1741, 2014.
[108] J. Zhou *et al.*, "Versatile core–shell nanoparticle@ metal–organic framework nanohybrids: Exploiting mussel-inspired polydopamine for tailored structural integration," *ACS nano,* vol. 9, no. 7, pp. 6951-6960, 2015.
[109] Q. Yang *et al.*, "Regulating the spatial distribution of metal nanoparticles within metal-organic frameworks to enhance catalytic efficiency," *Nature communications,* vol. 8, no. 1, pp. 1-9, 2017.
[110] X. Y. Xu and B. Yan, "Novel photofunctional hybrid materials (alumina and titania) functionalized with both MOF and lanthanide complexes through coordination bonds," *RSC advances,* vol. 4, no. 73, pp. 38761-38768, 2014.
[111] Z. Xie, T. Li, N. L. Rosi, and M. A. Carreon, "Alumina-supported cobalt–adeninate MOF membranes for CO 2/CH 4 separation," *Journal of Materials Chemistry A,* vol. 2, no. 5, pp. 1239-1241, 2014.

[112] J. Gascon, S. Aguado, and F. Kapteijn, "Manufacture of dense coatings of Cu3 (BTC) 2 (HKUST-1) on α-alumina," *Microporous and Mesoporous Materials,* vol. 113, no. 1-3, pp. 132-138, 2008.
[113] T. Han, C. Li, X. Guo, H. Huang, D. Liu, and C. Zhong, "In-situ synthesis of SiO2@ MOF composites for high-efficiency removal of aniline from aqueous solution," *Applied Surface Science,* vol. 390, pp. 506-512, 2016.
[114] T. J. Bandosz and C. Petit, "MOF/graphite oxide hybrid materials: exploring the new concept of adsorbents and catalysts," *Adsorption,* vol. 17, no. 1, pp. 5-16, 2011.
[115] X. Zhou *et al.*, "Enhanced separation performance of a novel composite material GrO@ MIL-101 for CO2/CH4 binary mixture," *Chemical Engineering Journal,* vol. 266, pp. 339-344, 2015.
[116] R. Kumar, K. Jayaramulu, T. K. Maji, and C. N. R. Rao, "Hybrid nanocomposites of ZIF-8 with graphene oxide exhibiting tunable morphology, significant CO 2 uptake and other novel properties," *Chemical Communications,* vol. 49, no. 43, pp. 4947-4949, 2013.
[117] S. Liu *et al.*, "Nanosized Cu-MOFs induced by graphene oxide and enhanced gas storage capacity," *Energy & Environmental Science,* vol. 6, no. 3, pp. 818-823, 2013.
[118] O. M. Yaghi, M. O'Keeffe, N. W. Ockwig, H. K. Chae, M. Eddaoudi, and J. Kim, "Reticular synthesis and the design of new materials," *Nature,* vol. 423, no. 6941, pp. 705-714, 2003.
[119] G. Férey, C. Mellot-Draznieks, C. Serre, and F. Millange, "Crystallized frameworks with giant pores: are there limits to the possible?," *Accounts of Chemical Research,* vol. 38, no. 4, pp. 217-225, 2005.
[120] S. Kitagawa, R. Kitaura, and S. i. Noro, "Functional porous coordination polymers," *Angewandte Chemie International Edition,* vol. 43, no. 18, pp. 2334-2375, 2004.
[121] G. Férey, "Hybrid porous solids: past, present, future," *Chemical Society Reviews,* vol. 37, no. 1, pp. 191-214, 2008.
[122] N. A. Khan and S.-H. Jhung, "Facile syntheses of metal-organic framework Cu 3 (BTC) 2 (H 2 O) 3 under ultrasound," *Bulletin of the Korean Chemical Society,* vol. 30, no. 12, pp. 2921-2926, 2009.
[123] M. Schlesinger, S. Schulze, M. Hietschold, and M. Mehring, "Evaluation of synthetic methods for microporous metal–organic frameworks exemplified by the competitive formation of [Cu2 (btc) 3 (H2O) 3] and [Cu2 (btc)(OH)(H2O)]," *Microporous and Mesoporous Materials,* vol. 132, no. 1-2, pp. 121-127, 2010.
[124] J. Kim, S.-H. Kim, S.-T. Yang, and W.-S. Ahn, "Bench-scale preparation of Cu3 (BTC) 2 by ethanol reflux: Synthesis optimization and adsorption/catalytic applications," *Microporous and mesoporous materials,* vol. 161, pp. 48-55, 2012.
[125] Y.-R. Lee, J. Kim, and W.-S. Ahn, "Synthesis of metal-organic frameworks: A mini review," *Korean Journal of Chemical Engineering,* vol. 30, no. 9, pp. 1667-1680, 2013.
[126] A. Domán, S. Klébert, J. Madarász, G. Sáfrán, Y. Wang, and K. László, "Graphene oxide protected copper benzene-1, 3, 5-tricarboxylate for clean energy gas adsorption," *Nanomaterials,* vol. 10, no. 6, p. 1182, 2020.
[127] M. D. Abràmoff, P. J. Magalhães, and S. J. Ram, "Image processing with ImageJ," *Biophotonics international,* vol. 11, no. 7, pp. 36-42, 2004.
[128] J. Davis, K. Tiwari, and I. Novosselov, "Soot morphology and nanostructure in complex flame flow patterns via secondary particle surface growth," *Fuel,* vol. 245, pp. 447-457, 2019/06/01/ 2019, doi: https://doi.org/10.1016/j.fuel.2019.02.058.
[129] J. Davis, E. Molnar, and I. Novosselov, "Nanostructure transition of young soot aggregates to mature soot aggregates in diluted diffusion flames," *Carbon,* vol. 159, pp. 255-265, 2020/04/15/ 2020, doi: https://doi.org/10.1016/j.carbon.2019.12.043.
[130] Y. Chen *et al.*, "A new MOF-505@ GO composite with high selectivity for CO2/CH4 and CO2/N2 separation," *Chemical Engineering Journal,* vol. 308, pp. 1065-1072, 2017.

[131] S. Loera-Serna *et al.*, "Electrochemical behavior of [Cu3 (BTC) 2] metal–organic framework: The effect of the method of synthesis," *Journal of alloys and compounds,* vol. 540, pp. 113-120, 2012.

[132] J. M. Augustine, S. N. Maiti, and A. K. Gupta, "Mechanical properties and crystallization behavior of toughened polyamide-6/carbon nanotube composites," *Journal of Applied Polymer Science,* vol. 125, no. S1, pp. E478-E485, 2012.

[133] A. Gholampour, M. Valizadeh Kiamahalleh, D. N. H. Tran, T. Ozbakkaloglu, and D. Losic, "From graphene oxide to reduced graphene oxide: impact on the physiochemical and mechanical properties of graphene–cement composites," *ACS applied materials & interfaces,* vol. 9, no. 49, pp. 43275-43286, 2017.

[134] L. Ge, L. Wang, V. Rudolph, and Z. Zhu, "Hierarchically structured metal–organic framework/vertically-aligned carbon nanotubes hybrids for CO 2 capture," *Rsc Advances,* vol. 3, no. 47, pp. 25360-25366, 2013.

[135] X.-S. Wang, S. Ma, D. Sun, S. Parkin, and H.-C. Zhou, "A mesoporous metal− organic framework with permanent porosity," *Journal of the American Chemical Society,* vol. 128, no. 51, pp. 16474-16475, 2006.

[136] A. M. B. Furtado, J. Liu, Y. Wang, and M. D. LeVan, "Mesoporous silica–metal organic composite: synthesis, characterization, and ammonia adsorption," *Journal of Materials Chemistry,* vol. 21, no. 18, pp. 6698-6706, 2011.

[137] C. Petit, J. Burress, and T. J. Bandosz, "The synthesis and characterization of copper-based metal–organic framework/graphite oxide composites," *Carbon,* vol. 49, no. 2, pp. 563-572, 2011.

[138] S. J. Yang, J. Y. Choi, H. K. Chae, J. H. Cho, K. S. Nahm, and C. R. Park, "Preparation and enhanced hydrostability and hydrogen storage capacity of CNT@ MOF-5 hybrid composite," *Chemistry of Materials,* vol. 21, no. 9, pp. 1893-1897, 2009.

[139] K. P. Prasanth, P. Rallapalli, M. C. Raj, H. C. Bajaj, and R. V. Jasra, "Enhanced hydrogen sorption in single walled carbon nanotube incorporated MIL-101 composite metal–organic framework," *International journal of hydrogen energy,* vol. 36, no. 13, pp. 7594-7601, 2011.